Master's Degree in Astrophysics
2022-2023

Calibration of stellar feedback in cosmological simulations

Iñigo Juanikorena Berasategi

Tutors: Andrea Negri & Claudio Dalla Vecchia
San Cristóbal de La Laguna, 2023

Resumen

En los últimos años, las simulaciones cosmológicas, más concretamente las hidrodinámicas, se han convertido en una de las grandes bazas de la astrofísica y la cosmología para intentar entender los procesos de formación y evolución de las galaxias. Esto se debe, mayormente, a la accesiblidad temporal que las simulaciones ofrecen, ya que, en contraposición a las observaciones, las simulaciones permiten tener acceso a todas las características que definen al sistema en cualquier momento determinado.

En este contexto, el Grupo de Teoría del Instituto Astrofísico de Canarias ha implementado módulos hidrodinámicos sobre el código de N-cuerpos PKDGRAV3. Al tratarse de un código para simulaciones cosmológicas, las resoluciones utilizadas son del orden de millones de masas solares, lo que hace imposible que los procesos físicos que dan forma a la materia bariónica de la galaxia (formación y *feedback* estelar, formación de agujeros negros, etc.) puedan ser simulados. Por ello, es necesario implementar física de sub-red (*sub-grid physics*); modelos que proporcionan los efectos de estos procesos cuando no pueden ser resueltos y, por tanto, simulados. No obstante, es necesario calibrar la física de sub-red para que las caracterísiticas de las galaxias simuladas coincidan con nuestras observaciones del universo.

En este estudio, llevamos a cabo la calibración del *feedback* estelar de PKDGRAV3. A pesar de que el modelo implementado dependa de varios parámetros, el *feedback* se puede controlar correctamente determinando la eficiencia máxima ($f_{th,max}$) de la energía eyectada por las partículas estelares. Por ello, hemos creado 5 simulaciones con los siguientes valores para el parametro de máxima eficiencia: $f_{th,max} = 0.5, 1, 3, 5$ y 10. Estas simulaciones contienen 200^3 partículas tanto de materia oscura como de gas, en un volumen comóvil $(13.4\,\mathrm{Mpc/h})^3$. Todas las simulaciones comienzan con las mismas condiciones iniciales, por lo que las diferencias entre ellas son debidas, casi por completo, al diferente valor de la eficiencia. No obstante, cabe resaltar que, debido a las restricciones de tiempo de un proyecto como este, hemos desactivado los agujeros negros, y por tanto el *feedback* AGN en 4 de las 5 simulaciones. Solo $f_{th} = 5$ contiene agujeros negros, lo que nos permitirá valorar cómo afecta la falta de *feedback* AGN a nuestra calibración.

En este trabajo presentamos el proceso de calibración, empezando por una introducción donde ponemos de relieve la importancia de las simulaciones hidrocosmologicas en la actualidad, además de la necesidad de llevar a cabo calibraciones rigurosas para la física de sub-red. A continuación, presentamos la metodología utilizada durante el proceso. Empezamos describiendo el código, centrandonos especialmente en la implementación de la física sub-red. Tras describir la formación estelar y la acreción y *feedback* de los agujeros negros, desarrollamos en profundidad cómo se aplica el *feedback* estelar, además de dotar de sentido físico a los parametros computacional presentes en el código.

Tras describir el código y las simulaciones que hemos generado, nos centramos en el post-procesamiento de los datos obtenidos. Para ello, es necesario identificar las

galaxias existentes en cada simulación, utilizando para ello los algoritmos *Friends-Of-Friends* y *Subfind*. Por motivos obvios, una gran parte de los observables que tenemos en astrofísica están relacionados con la luminosidad emitida por los objetos celestes. Por ello, nos es necesario computar la luminosidad de las galaxias previamente identificadas. Por tanto, generamos espectros de rango amplio utilizando librerias espectrales. Además, definimos el límite de masa mínimo que un halo debe tener para ser considerado galaxia, y derivamos la luminosidad mínima correspondiente.

Uno de los observables más importantes a la hora de calibrar son la función de masas y luminosidades estelares de las galaxias (GSMF y GSLF de sus siglas en inglés, respectivamente). Llevamos a cabo un ajuste de estos utiliando inferencia bayesiana, por lo que presentamos los aspectos teóricos más relevantes de la estadística bayesiana y las cadenas de Markov en la última subsección de la metodología.

Para los resultados, tomamos como referencia los datos en $z = 0.1$, ya que existe literatura suficiente a este valor del redshift para poder llevar a cabo comparaciones con estudios observacionales. Nos centramos principalmente en 3 observables: la historia de formación estelar, la relación color-masa estelar y las ya mencionadas GSMF y GSLF. En la historia de formación estelar, observamos diferencias notables en la primera mitad del tiempo simulado, donde las eficiencias bajas permiten una formación estelar notablemente mayor. No obstante, encontramos que a partir de $z = 1$ casi todas las eficiencias convergen a un valor cercano a $\Psi \approx 0.1$ $[M_\odot/\mathrm{yr}\,(\mathrm{Mpc/h})^{-3}]$. $f_{th} = 5$ transforma ligeramente menos gas en estrellas, probablemente debido al feedback *AGN*. Comparamos los resultados de nuestras simulaciones con la función analítica de Madau. Presentamos también la relación color $g-r$ - masa estelar para las galaxias simuladas. Además, representamos esta misma relación y la historia de formación estelar de una galaxia determinada para ilustrar el efecto del *feedback* en la extinción de formación estelar. A través de esto obtenemos referencias cualitativas del funcionamiento de las simulaciones.

Llevamos a cabo dos ajustes para la GSMF y la GSLF; para la GSMF, limitamos la probabilidad a priori del parámetro M^* a $10^{11.5}$ $M_\odot$ y 10^{13} $M_\odot$. El primer caso limita notablemente el punto de inflexión de la función Schechter, mientras que el segundo no genera ninguna restricción sobre el ajuste. En el caso de la GSLF, hemos ajustado una función Schechter única y una doble. Terminamos los resultados mostrando los ajustes realizados junto con los valores obtenidos para los parámetros α, M^* y ϕ, además de sus incertidumbres y las *corner plots* que muestran su correlación.

En la última sección, presentamos nuestras conclusiones. Encontramos que $f_{th} = 5$ es la eficiencia que mejor simula la historia de formación estelar en la primera mitad del tiempo, pero después se aleja de la función de Madau más que el resto de eficiencias. Además, comparamos los parametros obtenidos de los ajustes de GSMF y GSLF con dos trabajos observacionales. Para la GSMF, encontramos que

el valor de referencia para la pendiente (α) se encuentra entre $f_{th} = 3$ y $f_{th} = 5$ para la función limitada en $10^{11.5}$, mientras que está muy cerca de $f_{th} = 5$ para el caso sin limitar. Para la GSLF, la referencia tambien ofrece un valor intermedio entre $f_{th} = 3$ y $f_{th} = 5$ para el Schechter único, mientras que se encuentra muy cercano a $f_{th} = 1$ y $f_{th} = 3$ cuando el ajuste se hace con un doble Schechter. Para M^*, vemos que, tanto para masas como para luminosidades, el punto de inflexión se encuentra en posiciones mucho menos masivas que las que hemos obtenido. Relacionamos esto con la desactivación de *feedback* de AGN, como nos indica que M^* sea notablemente más cercano al valor de referencia en $f_{th} = 5$.

Por último, presentamos dos sugerencias para futuras calibraciones. Primero, creemos que la presencia de agujeros negros haría que el análisis sea más riguroso, además de permitir analizar la degeneración entre ambos *feedbacks*. Para acabar, exponemos un método de inferencia bayesiana para hacer que la calibración sea cualitativamente más exacta.

Contents

1 Introduction

Cosmological simulations, particularly hydrodynamical simulations, have emerged as powerful tools in astrophysics for investigating the formation and evolution of galaxies. These simulations use computational models to recreate the large-scale structure of the universe and the physical processes that govern the formation and growth of galaxies.

A crucial aspect of hydrodynamical cosmological simulations is their ability to simulate the formation and evolution of galaxies in a self-consistent manner. Observational data provides us with information about a specific moment in the evolution of a certain galaxy, forcing us to make theoretical assumptions in order to reconstruct their unfolding throughout the life of the universe. On the other hand, simulations track the gravitational collapse of Dark Matter (DM) halos, the cooling of gas within these halos, and the subsequent formation of stars, giving us access to information of different features in any specific instant. By simulating these processes, we can study how galaxies grow and develop by tracking their evolution. In a certain way, we could say that these simulations act as virtual laboratories to explore and test theoretical models and make predictions for future observations.

Furthermore, hydrodynamical simulations allow us to probe the impact of various physical mechanisms on galaxy formation. For instance, we can study the effects of feedback processes such as stellar winds, supernovae, and Active Galactic Nuclei (AGN) on galaxy evolution. These simulations provide insights into the regulation of star formation, the enrichment of galaxies with heavy elements, and the growth of supermassive black holes at their centers.

1.1 Need for calibration

In the development of cosmological simulations, an essential step is the calibration of the simulation code to accurately reproduce observed astrophysical phenomena. Calibration involves fine-tuning the model parameters and incorporating empirical data to ensure that the simulated universe matches our understanding of the real universe. This process is crucial because it allows scientists to validate the simulation results and make meaningful comparisons with observational data.

Stellar feedback is a key process in galaxy formation and evolution, and its accurate representation in cosmological simulations is of paramount importance. Stellar feedback refers to the energy released by stars into their surrounding gas through various mechanisms, such as stellar winds, supernovae, etc. It plays a vital role in regulating star formation, shaping the interstellar medium, and driving galactic outflows. The stellar feedback, as well as other physical processes that baryonic matter undergo, cannot be resolved, so sub-grid implementations are needed. These are series of models that provide the effects of certain processes (star formation, BH formation, stellar feedback, etc.) when it is not possible to simulate them.

Calibrating the stellar feedback model in simulations involves matching the observed properties of galaxies, such as their Star Formation Rates (SFR), Stellar Mass and Luminosity Functions (GSMF and GSLF), and color-mass relations. This requires careful adjustment of feedback parameters to reproduce the desired level of star formation and gas distribution. The calibration process also relies on comparisons with observational data in order to reproduce faithfully our universe. By refining the feedback model, we can achieve simulations that capture the observed properties of galaxies across a wide range of time intervals.

Resolution, or the level of detail in a simulation, also plays a crucial role in the calibration process, particularly for capturing the effects of stellar feedback. Higher resolution simulations allow for better resolving individual star-forming regions, supernova explosions, and the resulting energy injection into the surrounding gas. This increased resolution leads to a more accurate representation of feedback processes, enabling a more realistic reproduction of galaxy properties. However, achieving high resolution comes at a computational cost; simulating a larger volume with higher resolution requires significant computational resources, which are out of reach with current technology if we want to reproduce a significant fraction of the universe.

In summary, calibration of the sub-grid physiscs is a vital step in the development of cosmological simulations, ensuring that the simulated universe accurately reflects observational data. Calibration of stellar feedback is of particular importance, as it influences the regulation of star formation and the overall evolution of galaxies. Thus, correctly calibrating simulation codes is necessary to achieve accurate and insightful simulations that deepen our understanding of galaxy formation and the cosmos in general.

1.2 Aim of the work

The *Theory Group* of the *Instituto Astrofísico de Canarias* has recently introduced hydrodynamics (Asensio et al., 2022) on top of the N-Body code PKDGRAV3 cosmological code (Potter et al., 2016). In this work, we aim to calibrate the stellar feedback sub-grid physics.

For this purpose, we run 5 simulations with different stellar feedback efficiency values in a $(13.4\,\mathrm{Mpc/h})^3$ volume, resulting in a resolution around $10^6\,M_\odot$. Due to time constrains for this thesis, Black Holes (BH) have been deactivated in order to speed up the runs and to provide us with enough simulations to accomplish a trustful analysis. Nevertheless, one simulation is performed with full physics, meaning that BHs are present, resulting in AGN feedback also playing a role alongside stellar feedback. This will help us understand how the lack of AGN feedback affects our analysis and calibration.

Throughout the following work, we first introduce the methodology applied trough the calibration process in section 2. Here, we give some insight of the physics

on the code (section 2.1), followed by a overview of the post-processing (2.2) and a introduction to the methods applied in Bayesian fitting (2.3). After, we present our results in section 3, which are mainly centered around the Star Formation History (3.1), the color-stellar mass relation (3.2) and the fitting of the GSMF and GSLF via Markov Chain Monte Carlo (MCMC) methods (3.3). Finally, we draw our conclusions in section 4, using the results to assess the pros and cons of each efficiency value and suggesting improvements for future calibration processes.

2 Methodology

In this section, we will introduce the different algorithms and numerical codes that have been employed to run and analyse simulations. In particular, we will present the *PKDGRAV3* code to perform hydrodynamical cosmological simulations, as well as the post-processing, in particular the galaxy selection criteria, the galaxy magnitude computation and the building of the mass and luminosity functions.

2.1 The code

The foundations of PKDGRAV were set in the first place in Stadel (2001), where a new method to run N-body simulations has been described. Potter et al. (2016) presented a new version of the code, PKDGRAV3, where the computationally expensive parts were ported on GPUs, thus greatly improving the performances. This is currently one of the most efficient N-body sowftwares available; Potter et al. (2016) performed the largest simulation (at that time) of 2 trillions of particles, which took only 80 hours to reach $z = 0$, later surpassed by the EUCLID Flagship V2 (Euclid Collaboration et al., 2021) simulation arriving at 4 trillions of particles. One of the most extensive simulations of the large-scale structure of the universe was carried out with it (Knabenhans et al., 2019).

The original PKDGRAV3 code is a N-Body code, thus not being suitable to study galaxy formation and evolution. In this context, the *Theory Group* in the *Instituto Astrofísico de Canarias* decided to adopt this code as a base, and implement hydrodynamics and galaxy formation and evolution physical modules, e.g., cooling, star formation, supernova feedback, black hole accretion, etc. To achieve this, a quasi-Langrangian formulation is used; the gas is discreticed in individual gas particles, but fluid equations are solved with the meshless finite mass method (Hopkins & Raives, 2015), based on the work of Lanson & Vila (2008a,b). For a full description of the hydro solver implemented, see Asensio et al. (2022).

On the first place, there are usually dark matter and gas particles (also called Smoothed-Particle Hydrodynamics, SPH) with certain initial conditions, which, in PKDGRAV3, can be introduced as an external file or created at the beginning of the simulation given a seed. In our case, all the simulations have been created with

the same amount of particles (information related to this can be seen in table 1) and the same seed, so the initial conditions are equal for every simulation. They are created using a second-order Lagrangian perturbation theory following Crocce et al. (2006).

Once the simulations begin, the dark matter particles interact between themselves and with other particles only gravitationally, but the describing parameters of the gas particles change via hydrodynamic interactions. The typical resolution is $10^6\ M_\odot$, so small scale physical processes cannot be simulated, e.g., star formation or stellar feedback. To include it, we need sub-grid physics, which are series of models that provide the effects of the physical process we cannot simulate, e.g., a gas particle is transformed in a Single Stellar Population (SSP) of a certain mass. Under certain density and metallicity conditions, following Schaye & Dalla Vecchia (2008), these gas particles become stellar particles. Furthermore, black hole particle seeds are placed in the center of the galaxies when they reach a mass over $10^{10}\ M_\odot/h$, as done in Springel et al. (2005).

In general, the different sub-grid processes taken into account in the simulations are: radiative cooling, reionisation, star formation, stellar mass loss and metal enrichment, energy feedback from star formation, BH formation and accretion and AGN feedback. For this work, we will be describing the star formation, the AGN feedback and the stellar feedback, focusing mainly in this last one because the main objective of this project is calibrating this process. The rest of the processes are important for the evolution of the simulations, but they are also less linked to the stellar feedback calibration.

2.1.1 Star formation

In cosmological simulations, a stellar particle does not represent a single star due to the low mass resolution. Instead, it is represented by a single stellar population, massive particles that inherit the properties of the parent gas. The formula to compute star-formation rate (SFR, amount of gas mass that is converted into stars per unit time), which tries to reproduce the Kennicutt-Schmidt law, can be written in terms of pressure as

$$\dot{m}_* = m_g A \left(1 M_\odot\ pc^{-2}\right)^{-n} \left(\frac{\gamma}{G} f_g P\right)^{(n-1)/2}, \tag{1}$$

where m_g is the mass of the gas particle, $\gamma = 5/3$ is the adiabatic coefficient, G is the gravitational constant, f_g is the mass fraction of gas and $A = 1.515 \times 10^{-4}\ M_\odot\ \mathrm{yr}^{-1}\ \mathrm{kpc}^{-2}$ and $n = 1.4$ are constants set to reproduce a Chabrier Initial Mass Function (Chabrier, 2003). The conversion of a gas particle in a stellar one is a stochastic process; a particle has a probability equal to

$$\min\left(\frac{\dot{m}_* \Delta t}{m_g}, 1\right) \tag{2}$$

to become a SSP, where $\dot{m}_*$ is the star formation-rate and Δt is the time step of the simulation. Two conditions are set in order to ensure that the features of the gas are similar to the star-forming interstellar cold molecular gas; a gas particle must be denser than (Schaye et al., 2010)

$$\overset{*}{n}_H(Z) = 0.1 \left(\frac{Z}{0.002}\right)^{-0.64} \text{cm}^{-3} , \tag{3}$$

where Z is the gas metallicity (Schaye et al., 2010), and under a temperature $T_{eos}(\rho_g)$, set by the equation of state $P \propto \rho_g^{4/3}$ and normalized to $T_{eos} = 8 \times 10^3\ K$ at $n_H = 10^{-1}\text{cm}^{-3}$ (where n_H is the number density of hydrogen and ρ_g is the mass density of the gas). Gas particles with densities and temperature corresponding to $log\ T < log\ T_{eos} + 0.5$ and $n_H > \overset{*}{n}_H(Z)$ will transition with a probability set by equation (2).

2.1.2 BHs accretion and AGN feedback

Black Holes are widely considered to be one of the main players in galaxy formation and evolution (Kormendy & Ho, 2013). BH creation and evolution is a multiscale physical process that cannot be captured at the resolution of hydrodynamical simulations. Instead, we use sub-grid physics to create a BH, to simulate its accretion process and the subsequent Active Galactic Nuclei feedback. In hydro cosmological simulations, BHs are subject to three different processes: seeding, accretion and feedback.

BH seeding is performed by converting the star forming gas particle with the lowest potential energy in a galaxy into a BH particle when the halo's mass exceeds $10^{10}\,M_\odot$/h, with an initial mass $M_{BH} = 10^5\,M_\odot$/h. Once a BH is seeded, it can start growing in mass by accreating nearby gas particles, with an accretion rate equal to $\min(\dot{m}_{Edd}, \dot{m}_\text{B})$, where $\dot{m}_{Edd} = \frac{4\pi G m_{BH} m_p}{\epsilon_r \sigma_T c}$ is the Eddington mass acretion rate, and $\dot{m}_\text{B}$ is the Bondi accretion rate (Bondi & Hoyle, 1944).

AGN feedback is implemented in a stochastic thermal way, but this method is conceptually equal to the stellar feedback (explained in section 2.1.3). The energy injection rate is $\epsilon_f \epsilon_r \dot{m}_{accr} c^2$, where $\epsilon_r = 0.1$ is the typical value for the radiative efficiency of BHs and ϵ_f is the calibration parameter, analogous to f_{th}, which should be also calibrated.

However, BHs are important for quenching star formation in massive galaxies and are dominant in galaxy evolution at the massive end of the GSMF (Kormendy & Ho, 2013). Since the goal of this project is to calibrate the stellar feedback, we deactivate BH physics in all but a single run, corresponding to $f_{th} = 5$.

2.1.3 Stellar feedback

The main goal of this project is calibrating the stellar feedback in the new PKDGRAV3 code; i.e., deriving the correct values for the parameters that control the energy injected by stellar particles.

Stars are known to have a significant role in the creation of galactic structures via radiation, stellar-winds and, mainly, type II and type Ia supernovae (SN-II, SN-Ia). This way, the most massive stars formed in a SSP heat up the ISM and can possibly drive galactic-outflows of the ISM, thus quenching star formation. Therefore, including this effect is vital in order to model galaxy formation and evolution correctly, specially at low stellar mass, where stellar feedback plays a dominant role. Various approaches have been made during recent years, but what creates consensus is the fact that subgrid physics implementations are required to avoid the "overcooling" problem.

Historically, simulations have not been able to implement correctly stellar feedback; the efficiency of the transmission of energy from stellar to gas particles has been low, creating issues in energy conservation and preventing simulated galaxies from correctly achieving observed properties. According to Dalla Vecchia & Schaye (2012), the fundamental reason behind this is that the energy released is deposited in too many gas elements. Physically, SNII inject energy mechanically in their nearby gas (in a mass of few $M_\odot$), which later produces large temperature increases ($\Delta T \sim 10^8\, K$) around it via thermalization of the ejecta. On the other hand, when, in a simulation, energy is deposited in neighbour gas particles, the amount of mass heated is much larger, deriving in much smaller temperature jumps (ΔT). When each gas particle is heated by $\Delta T \sim 10^5 - 10^6\, K$ the energy is radiated back very quickly, often in less than a time-step, producing a big reduction in the efficiency of the process. Quantitatively, this is usually calculated relating the cooling-time of the gas particles with their sound-crossing time (the time that takes for a mechanical perturbation to cross the resolution element). In this context, augmenting the resolution (smaller particles) helps keeping better efficiencies, but does not solve the problem fundamentally.

In this work, the stellar feedback is implemented in a thermal and stochastic manner following Dalla Vecchia & Schaye (2012). The general idea is rather simple: instead of dividing the energy released by the SSP between all the neighbours (therefore giving each of them a small temperature jump), every neighbour has a certain probability to be heated up by a fixed amount ΔT.

Assuming that stars in the range $6 - 100\, M_\odot$ explode as SNII events releasing 10^{51} erg (Chiosi et al., 1992) and a Chabrier IMF, $8.73 \times 10^{15}\, \mathrm{erg\, g^{-1}}$ of stellar mass formed in a SSP should be released as stellar feedback energy to the SPH particles. This energy, in physical units, is freed 3×10^7 yr after the creation of the stellar particles, corresponding to the maximum lifetime of stars that undergo SNII explosion. Therefore, we can set a ΔT in order to minimize numerical losses due to overcooling,

and define f_{th}: the fraction of the total amount of energy from SNII per unit stellar mass that is injected on average in the stochastical process. In the most simple case, $f_{th} = 1$, the average energy per unit mass injected will be, as we have previously noted, 8.73×10^{15} erg g^{-1}. But as this theoretical calculations are not enough to assure the correct functioning of the simulations, finding the most suitable value for f_{th} is vital and the main objective in this project.

The detailed implementation of the stochastical feedback is done as follows: when a star particle is set to free its feedback energy, every neighbour particle is awarded with a $0 \leq r \leq 1$ random number. The gas particles will receive the energy, and therefore get a ΔT temperature jump, if $r \geq p$ is fulfilled. A formal derivation of the value of p can be observed in Schaye & Dalla Vecchia (2008), but, in short, this parameter is set by requiring the mean energy received by SPH particles to be equal to that liberated by the SSPs. This way,

$$p = f_{th} \frac{\epsilon_{\mathrm{SNII}}}{\Delta\epsilon} \frac{m_*}{\sum_{i=1}^{N_{ngb}} m_i} \ , \tag{4}$$

where $\epsilon_{\mathrm{SNII}} = m_* \, 8.73 \times 10^{15}$ erg g^{-1} and $\Delta\epsilon$ are the total available energy in the SSP and the energy jump in the SPH particles (related to ΔT), m_* is the mass of the star particle, N_{ngb} is the number of neighbours and m_i the mass of each of these ones. Overall, the mean total number of heated gas particles is,

$$< N_{heat} > \approx 1.3 f_{th} \left(\frac{\Delta T}{10^{7.5}} \right)^{-1} \ . \tag{5}$$

In the code, $\Delta T = 10^{7.5}\ K$ is set, which is a suitable value and it simplifies equation (5) to $< N_{heat} > \approx 1.3 f_{th}$.

Once all the sub-grid physics depends only on the free parameter f_{th}, there is one last effect to account for: the dependence of f_{th} on the local conditions. Cooling functions, and therefore stellar feedback, are dependent on the metallicity, as the cooling via metal lines are usually larger than pure H and He lines. Nevertheless, at high redshifts, where galaxies are generally less metallic and densities are high, feedback seems to be too inefficient (Schaye et al., 2015). Because of that, another dependence on the local density is added to compensate the initial losses at high densities, leading to the following expression for the feedback efficiency parameter,

$$f_{th} = f_{th,min} + \frac{f_{th,max} - f_{th,min}}{1 + \left(\frac{Z}{0.1 Z_\odot} \right)^{n_Z} \left(\frac{n_{H,Birth}}{n_{H,0}} \right)^{-n_n}} \ . \tag{6}$$

Here, Z and $Z_\odot = 0.0127$ are the stellar particle's and solar metallicities respectively, $n_{H,Birth}$ is the gas density at birth and the following values are set: $n_{H,0} = 0.67$ cm^{-3}, $n_Z = n_n = 2/ln10 = 0.87$. $f_{th,max}$ and $f_{th,min}$ are the maximum and minimum efficiency parameters; we will have $f_{th} \approx f_{th,max}$ when $Z \ll$ and/or $n_{H,Birth} \gg$ and $f_{th} \approx f_{th,min}$ for the contrary. In an ideal situation, every parameter which is not set by the SSP particles themselves, $n_{H,0}$, n_Z, n_n, $f_{th,min}$ and $f_{th,max}$, should be calibrated. But obviously, this would generate an unmanageable

degeneracy that would make the calibration unfeasible. In this context, the previously mentioned values are fixed, as well as $f_{th,min} = 0.5$, thus leaving $f_{th,max}$ as the only free parameter. The rest of values are taken from Schaye et al. (2015), where they were determined by a set of small tests.

This way, for a given $f_{th,max}$, the feedback parameter in equation (6) is represented by a sigmoid as a function of both stellar density ($n_{H,Birth}$) and metallicity (Z) parameters. In figure 1, we can see these dependencies for different values of $f_{th,max}$. Here, $f_{th,min}$ and $f_{th,max}$ set the minimum and maximum values, while the rest of assumed parameters control the form of the curve.

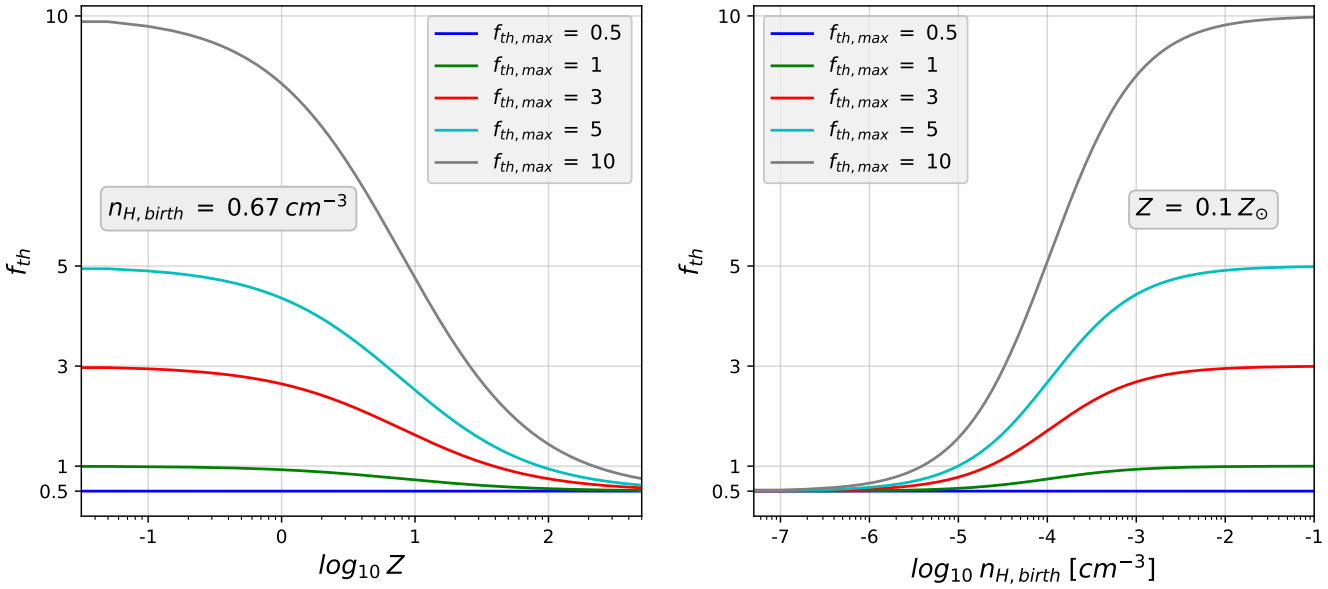

Figure (1) Dependency of the stellar feedback efficiency parameter with respect to parent gas metallicity (left) and density (right). On the left, density is fixed to $n_{H,Birth} = 0.67\,\mathrm{cm}^{-3}$, on the right, metallicity fixed to $Z = 0.1\,Z_\odot$. f_{th} is shown for 5 different values of $f_{th,max}$, colors indicated in the boxes.

Things like that, we have just set the fundamental pillars of our project; the feedback energy from stellar particles is controlled by a single parameter, f_{th}, that itself depends just on $f_{th,max}$. Our challenge is now creating simulations with different values for $f_{th,max}$ and analysing the results in order to find the most suitable choice. In Schaye et al. (2015), the final value chosen was $f_{th,max,EAGLE} = 3$, but there is no reason why that should also be applied to the new hydrodynamic PKDGRAV3 code. Due to time limitations, we have run 5 simulations with the following values: $f_{th,max} = 0.5, 1, 3, 5, 10$.

2.2 Galaxies selection and magnitude generation

In this section, we introduce the galaxies identification and their selection criteria. We will also give a general explanation on how the galaxy stellar luminosities in different bands are computed; we adopted magnitudes instead of flux in order to be consistent with current literature.

To identify galaxies in a snapshot, we apply the well-known Friends-Of-Friends (FOF) (Davis et al., 1985) and Subfind algorithms (Springel et al., 2001), incorporated in Gadget4 (Springel et al., 2021). When identifying individual galaxies, we impose a minimum of 32 DM particles per subhalo in Subfind. For our studies here we consider a galaxy subhalo having a total stellar mass $M_* > 6.1 M_\odot$, corresponding to 100 stellar particles. This number, yet arbitrary, sets a reasonable lower limit to what we consider a galaxy.

We follow Negri et al. (2022) for the magnitude generation process. We post-processed all stellar particles bound to galaxies in a series of apertures to test the correctness of the simulation. Nevertheless, the mass of the star particles, when generated, is similar to that of their parent gas particle, i.e., $M_{part,*} \sim 10^6\ M_\odot$. In low redshifts as $z = 0.1$, as the SFR is orders of magnitude smaller than in high redshifts (see figure 4), the low resolution of the SSPs introduces a big stochasticity in the star formation process. Because of that, all the SSPs with ages < 100 Myrs are transformed back into their parent gas particle, which is then resampled by $10^4\ M_\odot$ star particles with ages randomly selected in the range $6.3 - 100$ Myrs. The resampling process reduces the randomness of the star formation, leading to smoother magnitude computations.

A star particle in the simulation is characterized by its metallicity, age and initial mass. We adopted the Chabrier initial mass function in the computation, as in the simulations, and we employed the E-MILES (Vazdekis et al., 2016) stellar spectra library and Padova isochrones (Girardi et al., 2000) to compute the emitted spectrum for each stellar particle. This is done in a wide spectral range $\lambda \sim 1680\ \mathring{A} - 5\ \mu$m (from far UV to mid-IR). Afterwards, the fluxes of every star particle in each galaxy are summed up to compute the galactic spectra. We then convolve the spectrum with the response curve of the SDSS (Fukugita et al., 1996) and 2MASS (Cohen et al., 2003) filters to obtain the galaxy broad band luminosities. More specifically, we used the K_s filter of 2MASS for the limiting magnitude calculations and the g and r filters for the rest of the analysis (centered in $\lambda_{g,cen} \sim 4770\ \mathring{A}$ and $\lambda_{r,cen} \sim 6230\ \mathring{A}$ respectevely).

For limiting magnitude calculations, we use the total magnitude in the 2MASS K_s band which is centered in the infrared (IR) part of the spectrum ($\lambda_{K,cen} \sim 21600\,\mathring{A}$). After trying some filters in higher energy ranges, we have seen that this election leads to a relation with smaller dispersion in figure 2. Galaxies, overall, have more consistent emissions in the IR because this range is less sensitive to younger stellar populations than the UV or visible bands, thus there is less spread in magnitude

between young and old galaxies. This way, our discrimination is less subjected to stellar formation and other processes, and accounts more correctly for the mass of the galaxy.

We divide the magnitude range ($-26.1 \lesssim K_s \lesssim -13.5$ for all efficiencies) of all the galaxies in 30 bins, and distribute them in a K_s *vs* M_* relation. This way, the lower magnitude limit is set by the faintest bin in which the individual mass of the 95% of galaxies is greater than the $100 \times M_{part,gas}$ limit previously set. This yields a result of $K_{s,lim} \approx 19.15$, which we will use as a limit in the analysis over magnitudes. Figure 2 shows the K_s *vs* M_* relation with the limits in mass and magnitude superimposed.

However, we will not use the infrared K_s magnitude in our analysis, but the r band. Because of that, we want to translate $K_{s,lim} \approx 19.15$ into the later, in order to use it as a lower limit for our GSLF fits. For that, we plot the r magnitude of each galaxy with respect to K_s and perform a linear fit. This way, the value of r where the the linear fit and $K_{s,lim}$ intersect will be our limiting magnitude r_{lim}. This values are quite different between simulations, so we have decided not to take the mean and use a different limit for each efficiency. These linear fits are shown in figure 3.

2.3 Bayesian mass and luminosity functions

Bayesian inference is a statistical framework that allows us to compute parameter values by combining prior information with actual data. It employs Bayes' theorem (Gregory, 2005; van de Schoot et al., 2021) to calculate the posterior distribution, which represents the updated probability of the parameters. The likelihood represents the probability of observing the data given specific values of the parameters, and is commonly defined by previous theoretical knowledge. The evidence is the probability of observing the data averaged over all possible values of the parameters, and it serves as a normalization term. Finally, the prior represents our knowledge on the implemented model, meaning that we specify it independently with respect to the data in order to set theoretical limits to the parameters. Bayesian inference provides a way to gather all these to quantify uncertainty and make probabilistic predictions on the model parameters. Bayes' theorem is stated as:

$$f(\theta|x) = \frac{f(\theta)f(x|\theta)}{f(x)} \tag{7}$$

where $f(\theta|x)$ is the posterior, i.e. the probability of the model and the parameter θ given the data x, $f(x|\theta)$ is the likelihood, which is the probability of the data x given the model and the parameter θ and $f(\theta)$ is the prior. The denominator $f(x)$ is the evidence, and it is the integral of the nominator over all the parameter space (in Bayesian terms is marginalized):

$$f(x) = \int f(\theta)f(x|\theta)d\theta \ . \tag{8}$$

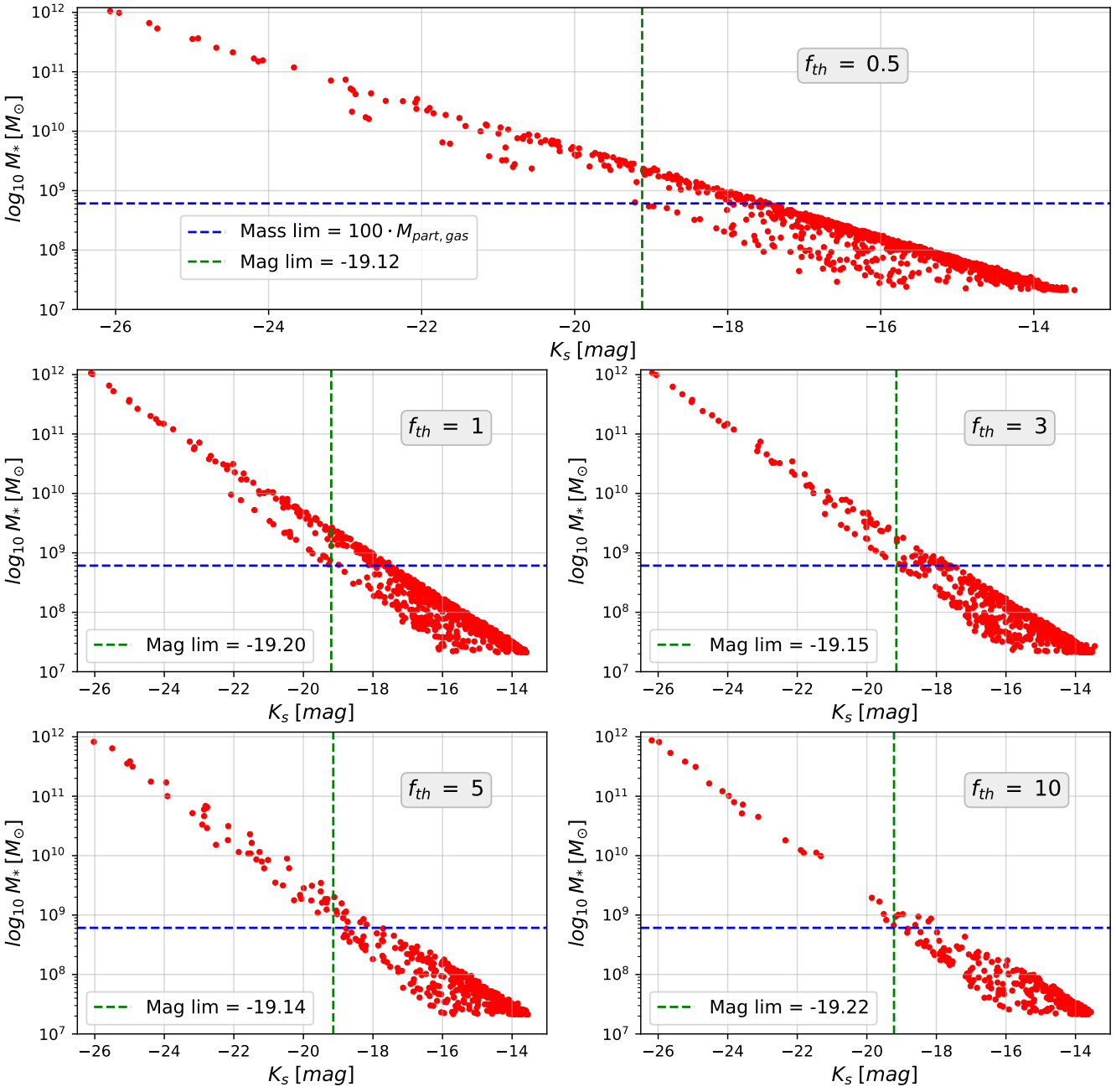

Figure (2) Magnitude Ks - stellar mass relation for every simulation at $z = 0.1$. The blue horizontal line represents the limiting mass $M_* = 100 \cdot M_{part,gas}$ and the green vertical line the corresponding magnitude $K_{s,lim}$ (see section 2.2). The efficiency of each simulation and the limiting values are shown in the boxes. The limit in mass is the same in every case.

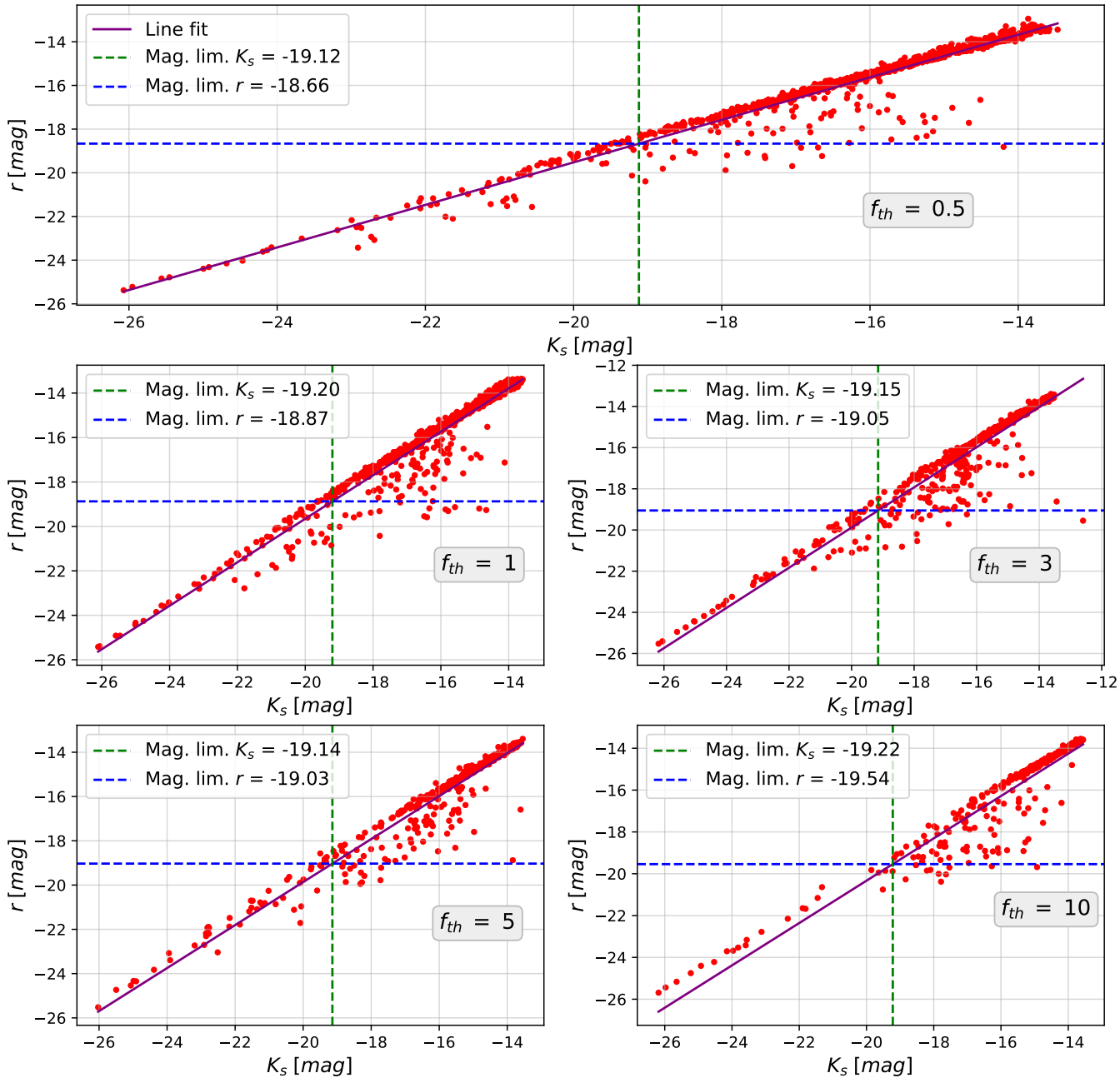

Figure (3) Ks - r relation for every galaxy and simulation at $z = 0.1$. The blue horizontal line represents the limiting magnitude $K_{s,lim}$ and the green vertical line the corresponding value of r (see section. The diagonal purple line is represents the linear fit 2.2). The efficiency of each simulation and the limiting values are shown in the boxes.

The evidence is a constant, and it can be neglected when applying bayesian inference, while it is of great importance while doing model selection, which we will not treat here.

In this section, we give a brief, qualitative explanation on how Markov chain Monte Carlo fitting works, and how we apply it to compute mass and luminosity functions. We follow the approach of Andreon et al. (2005) and Negri et al. (2022). We should also point out that, to fit GSMF and GSLFs, the data is usually binned, each bin is assigned a Poisson error (i.e. $\sqrt{N}$ where N is the number of counts) and the histogram is then fitted with a Schechter function. With this method, the number of data points is reduced significantly, leading to biases and loss of information. In addition, if a bin has a single count, the error in the logarithmic representation diverges to $\log(\sqrt{N=1}) = -\infty$, further complicating the representation of uncertainties. For this reason, we choose to apply bayesian inference in our work.

MCMCs are one of the most commonly used methods in bayesian statistics to explore the posterior distribution. In our case, we will restrict ourselves to bayesian inference, where the Bayes theorem is used to infer the best fit parameters of a distribution and their uncertainties. For both the GSMF and the GSLF, we will assume a Schecter function (we will dig into it in section 2.3.1), which needs 3 parameters (5 in the case of the double Schecter) to be univocally described.

The main objective now is to determine the posterior distribution function; the value of the parameters (and their uncertainties) so that the fitted function is most likely. Following Andreon et al. (2005), we apply the Extended Maximum Likelihood method here, where the extended likelihood for the Schechter function is defined as,

$$ln\,\Lambda = s + \sum_{i=1}^{N_{gal}} \ln p(M_i) \qquad ; \qquad s = -\int_{M_b}^{M_f} p(M)\,dM\ . \tag{9}$$

Here, M_i is the luminosity of the ith galaxy, N_{gal} is the number of galaxies, s represents the expected number of galaxies given the model, which is calculated integrating the extended probability $p(M)$ between two limiting magnitudes M_f and M_b, the faint and bright, respectively. $p(M_i)$ is the extended probability (not normalized to 1) of the ith galaxy of having a magnitude equal to M_i. $p(M) = V\,\Phi(M)$ with $V = (13.4\mathrm{Mpc/h})^3$ is the simulation volume, and Φ is the distribution function, in our case a Schechter (section 2.3.1).

Once the likelihood is set, MCMC is applied in the following way: an initial point in the parameter space is provided, and the MCMC starts to explore the posterior. In the next iteration, each parameter is awarded a nearby value to the previous one ($\vec{\theta}_{new}$) and the new likelihood is computed (Λ_{new}). After this, a random number ($rand$) from a flat distribution between 0 and 1 is created, and the chain will take the new values (Λ_{new}) if,

$$rand < \frac{\Lambda_{new}}{\Lambda_{old}}\ . \tag{10}$$

Obviously, if the likelihood is bigger with the new parameter values, the chain will jump to them. Instead, if the likelihood is smaller, the chain will jump or remain with a *rand* probability. This is applied because, at the end of the day, we want to find the parameter values that set the total maximum likelihood, but local maximums exist. On the one hand, if the current value is the total maximum, the parameter will fluctuate around it; but, if it is a local maximum, at some point, the chain will go far enough so that the tendency in the following iterations will lead to the total maximum. This can be done with multiple walkers at once.

A prior sets the range of values where each of the parameters can have a non-zero probability. In our case, we have set flat priors, meaning that, around the current value, any other number has the same probability of being assigned. Nevertheless, we have limited the parameter space in some parameters due to physical motivations (see section 2.3.1).

We employed 30 walkers with 10000 iterations, but the first 1000 are considered *burn-in* points and disregarded. This is done to be fairly independent on our first guess. To finalize, the median value of the parameters through the random walk is computed, which results in determining the posterior distribution.

2.3.1 GSMF and GSLF fits

First of all, we need to point out that, in all the simulations, we have excluded the central galaxies; in this case, the 7 most massive ones. These are formed in the centers of clusters, and their growth and evolution is driven by the immense mass accretion rates, lead by the fact that they are located in the center of huge gravitational wells. Anyways, central galaxies, being so massive, are barely affected by stellar feedback, so their role in our calibration can be disregarded.

Historically, the Galactic Stellar Mass Function and Luminosity Functions have been fit with a Schechter (1976) function. As we have previously indicated, we need 3 parameters to define the Schechter luminosity function, which is given by:

$$\Phi_1 = 0.4 \log(10) \phi 10^{0.4(\alpha+1)(M^*-M)} \exp -10^{0.4(M^*-M)} \, . \tag{11}$$

Note that, despite calling it *luminosity function*, we work with magnitudes. This later expression in terms of magnitudes can be derived from the original luminosity dependent one. This way, α is the slope at the faint end of the function, where the small-medium sized galaxies are located. The knee of the luminosity function is represented by M^*, and it sets the point where the LF transitions from a power law to an exponential cut-off. Finally, ϕ is just the normalization factor, which we consider the least interesting parameter in terms of physical consequences. In our case, we will use the stellar magnitude in the band r.

In the recent years, some observations showed that the steep end of the functions are not correctly fit by a single Schechter (Baldry et al., 2008; Blanton et al., 2005;

Li & White, 2009). In this work we also fit a double-Schechter function, assuming the knee magnitude is the same for the two components. This is given by:

$$\Phi_2 = 0.4\log(10)\exp -10^{0.4(M_2^*-M)} \left[\phi_b 10^{0.4(\alpha_b+1)(M_2^*-M)} + \phi_f 10^{0.4(\alpha_f+1)(M_2^*-M)}\right] , \tag{12}$$

where the b and f subscripts represent the bright and the faint parts of the data, respectively. In this case, the fit is usually highly degenerate, and we do not expect it to be very useful in our conclusions, but it is done for the sake of completeness.

On the other hand, the galactic GSMF is treated in a similar way, also fitted with the same 3 parameters (α, M^*, ϕ). The Schechter function for masses is the same as in equation (11), it has the same functional form but the parameter values are different (M^* here represents the knee mass instead of the knee magnitude). In this second fit for galactic masses, we have decided to set 2 different priors. The reason is the following: our simulations lack AGN feedback, which increases the steepness at the large mass galaxy range. Thus, we expect the *knee* to move to brighter values, so we will analyse how the prior affects it. In this context, we have conducted 2 fits with a prior for M^* limited between $10^{8.5} < M^*/M_\odot < 10^{11.5}$ and $10^{8.5} < M^*/M_\odot < 10^{13}$ to test if the LF knee is dominated by the prior. The later one, taking into account we limit the minimum mass of galaxies at $6.1 \times 10^8 M_\odot \approx 10^{8.75} M_\odot$ and that we take out the central massive galaxies, sets virtually no restriction to M^*.

2.4 Fiducial values

Here we present a table with the different simulation efficiencies, cosmology values, values for the feedback parameters, etc.

Simulations					
$\mathbf{f_{th,max}}$	0.5	1	3	5	10
BHs activated	No	No	No	Yes	No
ΛCDM					
$\mathbf{h}$	0.6711	$\mathbf{\Omega_0}$	0.3	$\mathbf{\Omega_b}$	0.049
$\mathbf{\Omega_\Lambda}$	0.7	$\sigma_\mathbf{8}$	0.8288	$\mathbf{n_s}$	0.9624
Simulation values					
Box size	13.4 Mpc/h	**z range**	$49 - 0$	**Num. particles**	200^3
Stellar feedback					
$\mathbf{f_{th,min}}$	0.5	$\mathbf{Z_\odot}$	0.0127	$\mathbf{n_Z = n_n}$	0.87
$\mathbf{n_{H,0}}$	0.67 cm^{-3}	**IMF**	Chabrier	$\mathbf{\Delta T}$	$10^{7.5}$ K

Table (1) Table containing a summary of different values fixed for the simulations.

3 Results

We run 5 simulations, with efficiencies $f_{th,max} = 0.5, 1, 3, 5$ and 10, evolving them from $z = 49$ to 0. In order to compare with current literature, we decided to work with $z = 0.1$ data, as it is done in the calibration of EAGLE (Crain et al., 2015). In the following section, we will present the most significant results in the analysis of the simulations divided by observables. We show first the total Star Formation History, followed by the color-stellar mass relation and we discuss the effects of f_{th} on these. Finally, we present the Galactic Stellar Mass and Luminosity Function fits.

3.1 Total Star Formation History

The Star Formation History (SFH) measures the amount of mass converted from gas to stars per unit of time and volume throughout the evolution of the universe. In the context of cosmological simulations, this is easily computed by measuring how many gas particles are transformed into star particles in a time bin, weighted by their initial masses.

In first place, we calculate the SFH of the whole cosmological volume for each simulation in terms of redshift (and lookback time). The lookback time is calculated assuming the results of the Planck collaboration (and N. Aghanim et al., 2020), resulting in an age of the universe of 13.8 Gyrs. We show also the analytic Madau function (Madau & Dickinson, 2014) in order to compare our results (figure 4).

It is clear that all efficiencies start forming stars at $z = 10$, and scale in a similar

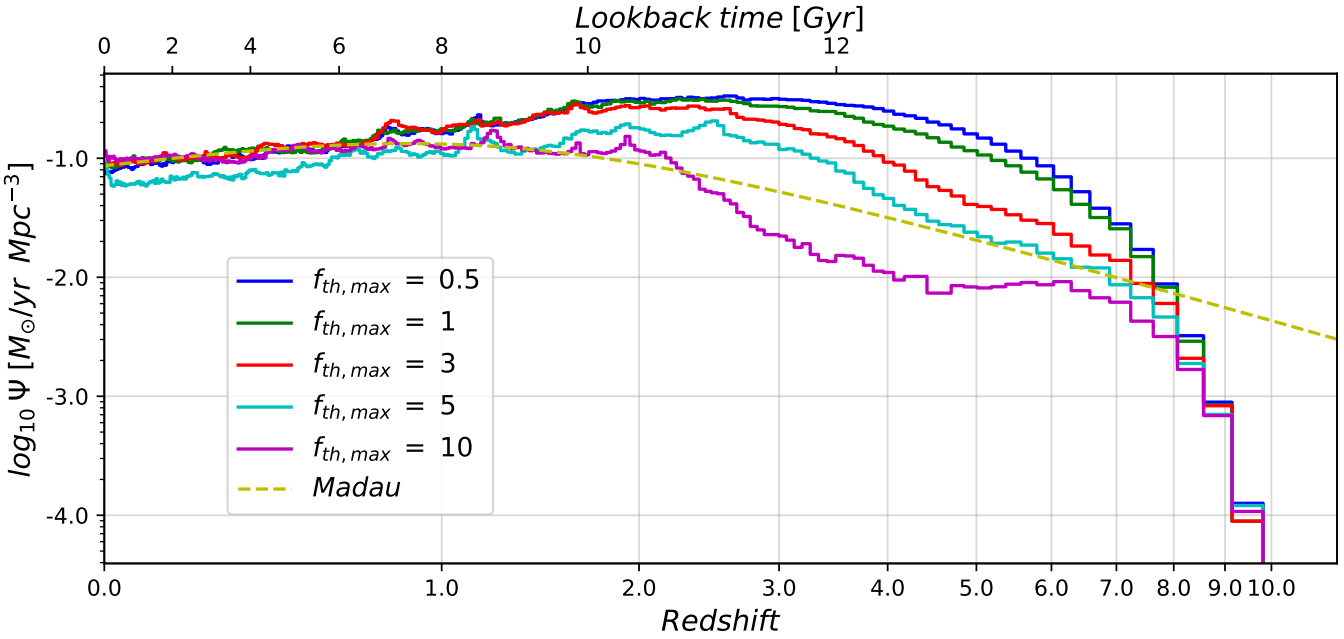

Figure (4) SFH for the whole volume for all the runs. The corresponding lookback time for each redshift is on the top axis. The analytic Madau function is overplotted in yellow. The box shows the color of the data in each simulation.

way for a short period of time. Afterwards, $f_{th} = 0.5$ and 1 keep increasing the SFR rapidly, while $f_{th} = 5$ and 10 prevent stars from forming, thus moderating the SFR. All the simulations hit their maximum SFR in the $z = 3-1$ interval, and later decrease softly. We can see that the low efficiency ones have a smoother evolution, while the high ones tend to be more bursty.

The analytic Madau model starts forming stars in higher redshifts, even before the beginning point of our simulations. In later stages, after $z = 1$, all the efficiencies converge to a value near $\Psi \approx 0.1$ $[M_\odot/\mathrm{yr}\ (\mathrm{Mpc/h})^{-3}]$. In the range $z = 7-3$, efficiency $f_{th} = 5$ seems to give the closest results to the analytic model, and from $z = 3-1$, before all simulations converge, $f_{th} = 10$ reproduces it best.

3.2 Color-stellar mass relation

In this section, we present the $g-r$ color - stellar mass relation for each simulation. The magnitudes in both bands correspond to the total mass. In this case, we will not exclude galaxies with $M_* < 10^{8.75}\,M_\odot$, but note that a big fraction of the objects are below this limit, see figure 5.

All the plots present a recognizable red sequence, but its extension in mass is shorter for higher efficiencies. The red sequence reaches almost $10^{10}\,M_\odot$ galaxies for $f_{th} = 0.5$ and 1, but ends before $10^9\,M_\odot$ for $f_{th} = 5$ and 10; in fact, there are barely any galaxies in the $10^9 - 10^{10}\,M_\odot$ range for the high efficiencies, where stellar feedback is most efficient. This shows how large efficiencies prevent medium sized,

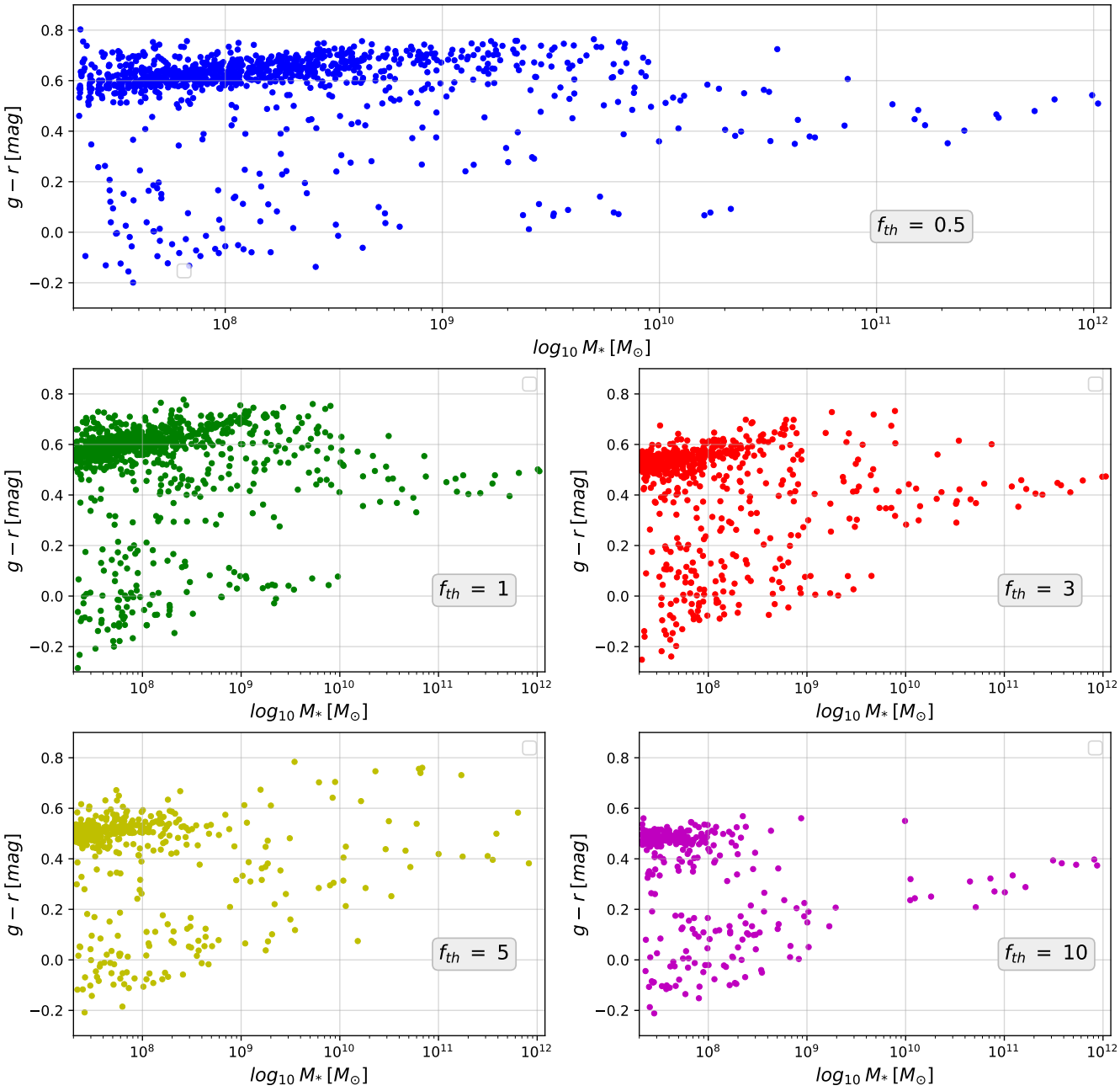

Figure (5) $g-r$ color-stellar mass diagram at $z = 0.1$ for all the galaxies. Galaxies magnitudes are computed inside an aperture of 2000 kpc. The efficiency of each simulation is shown in the boxes.

red galaxies from forming.

Red galaxies are overall older and quiescent, without almost any star formation. This is because the emission of small sized, long living stars is situated in the redder part of the spectrum in comparison to newly formed, massive ones, whose UV emission dominates their spectra. This is closely related to the SFH in figure 4; the difference in star formation rates is large in high redshifts, whereas it becomes negligible in later times. Moreover, the red sequence is not only shorter in mass for high efficiencies, but also bluer, as it is placed between $g-r=0.4-0.6$ for $f_{th}=5$ and 10 and between $g-r=0.5-0.8$ for $f_{th}=0.5$ and 1. $f_{th}=3$ is basically a transition case between both.

On the other hand, there is a visible blue cloud in all the simulations, which contains star-forming galaxies. The difference in this region is considerably smaller than in the red sequence, what can also be explained by the similar SFR in the late universe. Also, the blue cloud in high efficiencies is, although not more populated, more isolated because the green valley is almost nonexistent for $f_{th}=5$ and 10.

3.2.1 Color-stellar mass for individual galaxies

To better illustrate the effect of feedback on the color and stellar mass of red sequence galaxies, we have chose to follow 3 individual galaxies: a blue ($g-r=0.15$, $M_*=5.3\times10^9\ M_\odot$), a green ($g-r=0.48$, $M_*=2.8\times10^9\ M_\odot$) and a red one ($g-r=0.75$, $M_*=1.4\times10^9\ M_\odot$) in the $f_{th}=0.5$ simulation. After identifying this same galaxies in every simulation, we plot their individual color-stellar mass relation in figure 6.

In order to find the same galaxies in other simulations, we select the DM particles bond to the subhaloes and, identifying the particles by their IDs, we verify in which galaxy they are located in the rest of simulations. In this process, the 80th percentile of the particles were contained inside a galaxy with rather similar properties in the rest of simulations. There is one exception, the blue galaxy in $f_{th}=3$; most of its particles were located inside a massive central galaxy, so we have decided to disregard this case.

In figure 6 we see the individual transformation in the color of 3 galaxies when the efficiency is changed. In the red galaxy, we can observe the general behaviour mentioned earlier; when the efficiency is increased the color and the stellar mass decreases almost linearly, thus overall creating a shorter and bluer red sequence. On the other hand, the transformation of the green galaxy is less clear, there is not a clear relation in the change of color, but the stellar mass tends to decrease with efficiency. Finally, for the blue galaxy, the change seems to be almost random, without any clear pattern neither for color nor for mass.

The reason behind this can be understood similarly to that on section 6; smaller

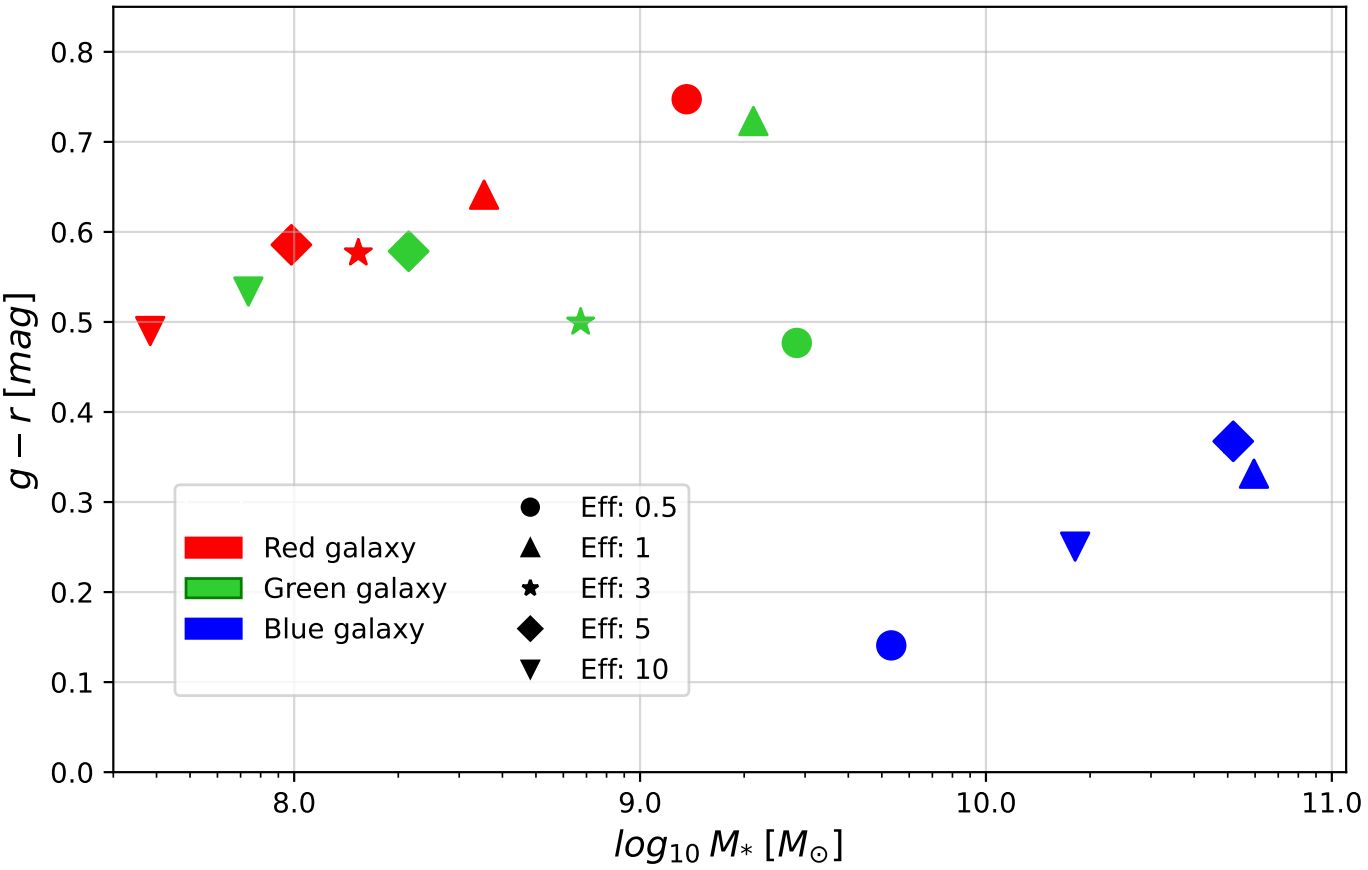

Figure (6) $g-r$ color-stellar mass diagram at $z = 0.1$ for 3 individual galaxies. The values in simulation $f_{th} = 0.5$ for each galaxy are: $g - r = 0.15$, $M_* = 5.3 \times 10^9\ M_\odot$ for the blue, $g - r = 0.48$, $M_* = 2.8 \times 10^9\ M_\odot$ for the green and $g - r = 0.75$, $M_* = 1.4 \times 10^9\ M_\odot$ for the red. Different markers represent different simulation, shown in the box.

SFRs in early stages induce old galaxies to form less star particles along larger periods of time, what turns into less total stellar mass and a bigger massive / non-massive star relation at $z = 0.1$. At low redshifts, the SFRs are much more similar for all the simulations, so the randomness in star formation creates a more chaotic behaviour in this relation.

3.2.2 SFH for a single galaxy

Here, we present the SFH for the red galaxy analysed in 3.2.1 at redshift $z = 0.1$. The graph is visible in 7, and the logarithmic SFR along the evolution of the galaxy in different simulations is represented in it. Note that this is a histogram, so the bins tend to make the graph more bumpy than the actual star formation evolution. Also, the line width increases with efficiency for the sake of visualization, but this has to be taken into account when analysing the duration of the star forming bursts.

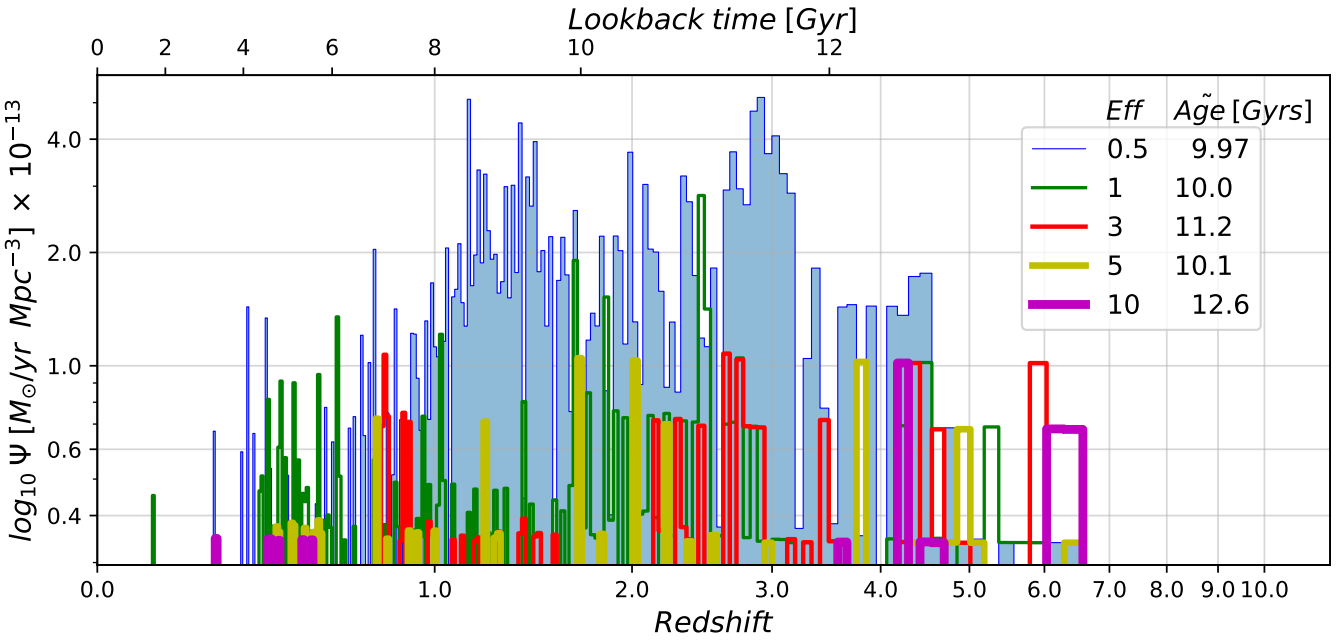

Figure (7) Individual Stellar Formation History at $z = 0.1$ for the red galaxy in figure 6. The color that represents each simulation is in the box alongside the median of the age of star formation. Note that the line width increases with efficiency and this can alter the perception of the width of bins.

We observe how, for the lowest efficiency, the star formation is continuous throughout its history. For $f_{th} = 1$, the formation is also almost continuous but notably smaller, thus producing less stars, and the same happens for $f_{th} = 3$; there exists star formation along the whole range but it has a more bumpy behaviour than the previous ones. For $f_{th} = 5$, the star formation is condensed in temporally separated bursts that tend to be similar to the $f_{th} = 3$ case but less frequent in time. Finally, $f_{th} = 10$ starts creating stars at the same time as the the rest, but after some bursts,

the galaxy is kept quenched until after $z = 1$.

This SFHs fit well with what we observe in figure 6, the integrated SFR, what basically equals the total stellar mass, is obviously larger for lower efficiencies. On the other hand, the later bursts in high efficiencies create bigger fractions of the total mass in later epochs, so the surviving massive stars make the whole galaxy bluer.

Regarding the physics of the system, this graph shows very well the behaviour of stellar feedback. After forming the first stars at the same time, high efficiencies displace surrounding gas considerably, quenching the star formation in later stages until the gas has time to gather and cool again. In fact, the feedback of the first stars at $f_{th} = 10$ inhibits formation for almost 6 Gyrs. Furthermore, when the efficiency of the feedback is low, less gas is heated up, cold gas is more abundant and the galaxy keeps forming stars continuously.

3.3 GSMF and GSLF fit analysis

In this section, we present the results of fitting the Schechter function to the mass and luminosity distributions for every simulation at $z = 0.1$. In the first place, we show two fits for the mass distribution; both are computed with flat priors, but the first one's prior is limited at $10^{11.5}\,M_\odot$ (narrow-prior) and the second one at $10^{13}\,M_\odot$ (large-prior). Afterwards, we present the luminosity functions fits with both a single and a double Schechter. As we have previously explained, we fit all the galaxies using bayesian inference, but the data is binned for representation alongside with Poissonian error bars. The line in the plot shows the Schechter function with the best fit parameter values. Also, we show shaded areas around the line delimited by the uncertainties of the parameter α. This helps visualize the uncertainty of the slope in each simulation and mass/magnitude range. All the best fit parameters are shown in table 2.

Concerning the priors, on the one hand, we set $-2.5 < \alpha$ in all cases. The $\Lambda-$Cold Dark Matter model predicts mass function is a power-law with slope -2 (Springel et al., 2008). Since stellar feedback flattens the faint end slope, we limit α to be larger than -2. On the other hand, we try limiting $M^* = 10^{11.5}\,M_\odot$ because of the nature of the simulations: as we do not apply AGN feedback, which produces the exponential cut off at the bright/massive end of the distribution, we expect the knee of the Schechter function to move towards a more bright/massive position. The stellar feedback drives the evolution of small galaxies, so in a simulation with AGN feedback activated, we would expect its inflexion point below $10^{11.5}\,M_\odot$.

Narrow-prior Mass Function

Figure 8 shows the mass function with the narrow prior. As expected, the knee is very close to the $M^* = 10^{11.5}\,M_\odot$ limit in all the simulations, so we are basically forcing the fit to change slopes in the same position for all cases. Corner plots for simulation $f_{th} = 0.5$ are shown in the left side in figure 10, where we can see the

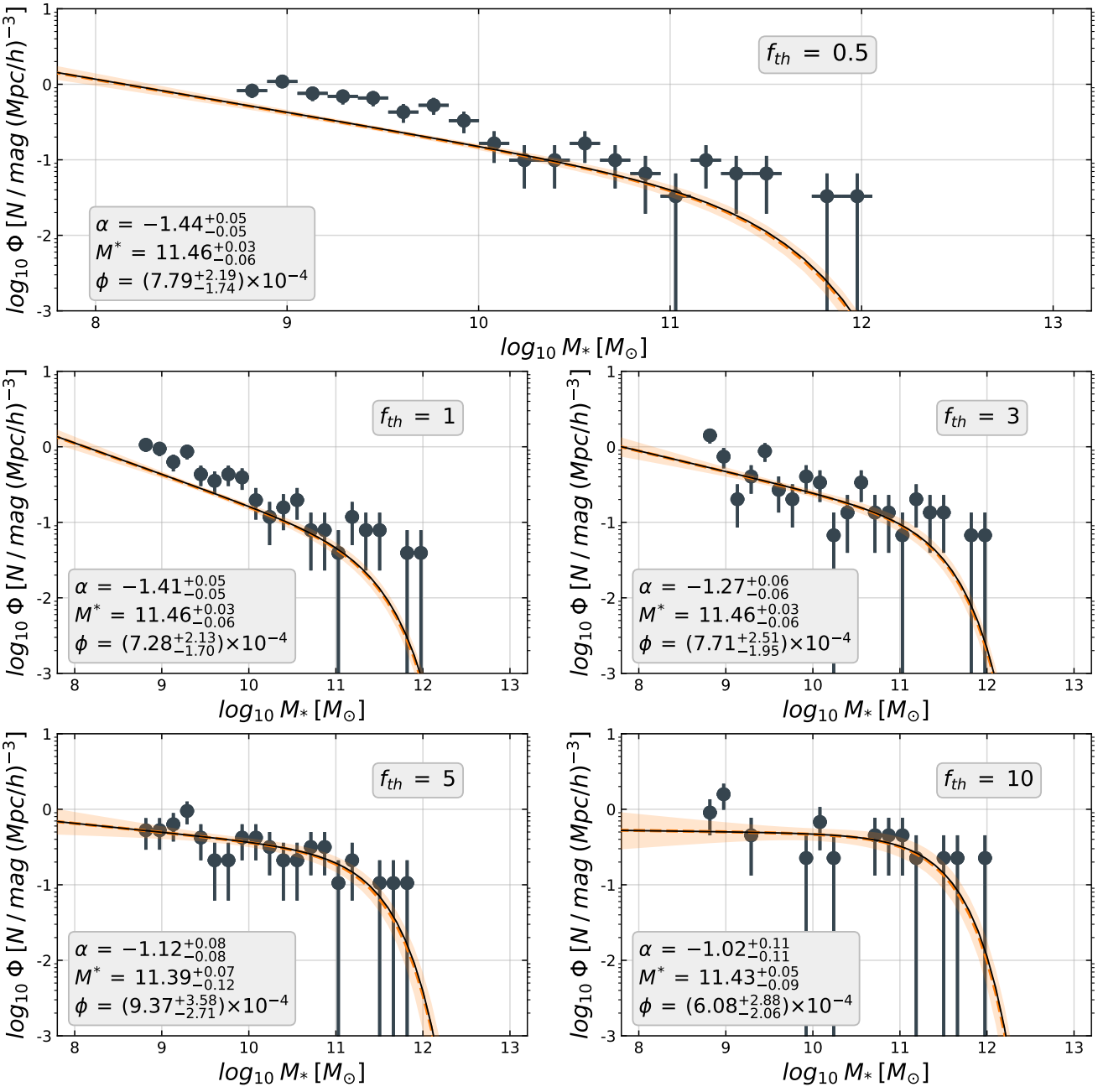

Figure (8) GSMF fits with narrow-prior at $z = 0.1$ for all the simulations. Fit is done using all data points, but binned for representation. Bars show Poissonian error for each bin. Shaded area is delimited by the uncertainties of α. Best fit values for parameters and their uncertainties are shown in the boxes.

posterior distributions and the crosss-correlations between model parameters. They clearly show the tendency of M^* to reach higher values than $M^* = 10^{11.5}\,M_\odot$ whatever the values of the rest of parameters are. M^* shows the same behaviour for the corner plots of the rest of simulations.

α spans the interval $[-1.45, -1.0]$, becoming flatter as the efficiency is increased. This is exactly what one should expect; stronger stellar feedback results in more medium mass galaxies in comparison to dwarfs because the ejected energy from individual SSPs is more efficient when there is less gas in the galaxy. In fact, for $f_{th} = 10$, the LF is almost flat until it reaches the knee, meaning that the amount of galaxies in all masses is almost equal in this range. The normalization parameter ϕ fluctuates without showing any clear tendency, as we could expect from its small physical meaning.

Large-prior Mass Function

In figure 9, we show the mass function fit with its prior limited to $M^* = 10^{13}\,M_\odot$, meaning that effectively we are not imposing any restrictions. Comparing to figure 8, we note that the knee has moved to higher mass positions, stabilising at $M^* \approx 10^{12}\,M_\odot$ for all the efficiencies apart from $f_{th} = 5$, since this is the only run with AGN feedback, which prevents the formation of massive galaxies. The slope α flattens with bigger efficiencies as in the previous fit, but it is steeper than the previous one in each individual simulation. One can notice that allowing a larger prior for the knee magnitude, as well as moving it to more massive positions, increases the faint end slope. The values for ϕ are now smaller and fluctuate less than in the previous case, except for $f_{th} = 5$, where the small change in the knee induces a more similar value to the previous fit. Moreover, the corner plot for $f_{th} = 0.5$ is shown in the right panel of figure 10. Here, we can see that M^* is no longer prior dominated.

The luminosity function fitted with a single Schechter can be seen in figure 11. Here, the behaviour of the distribution is opposite to the mass function due to the intrinsic negative definition of the magnitudes. The prior limits for α are equal to the previous case, and the upper limit for M^* is set at $r = -26$, again avoiding it to be prior dominated. On the other hand, the lower limit for magnitudes is different for each case as it was explained in section 2.2.

In this case, the behaviour of M^* is similar to the large-prior mass function; all knees except for $f_{th} = 5$ have similar values around -24.7, although more scattered than in masses. For $f_{th} = 5$, $M^* = -23.35$ is much closer to the faint part of the distribution, agreeing with the mass function that showed a change for the slope in smaller galaxies. The faint zone slope confirms the previous tendency of flattening with increasing efficiencies except for $f_{th} = 5$. This simulation seems to break with the gradual decline behaviour and shows a much flatter slope than $f_{th} = 10$, as well as a much bigger value for ϕ. Superior panel in figure 13 shows the corner plot for the $f_{th} = 0.5$ simulation. Here we can see the posterior distributions for each parameter and their cross-correlations.

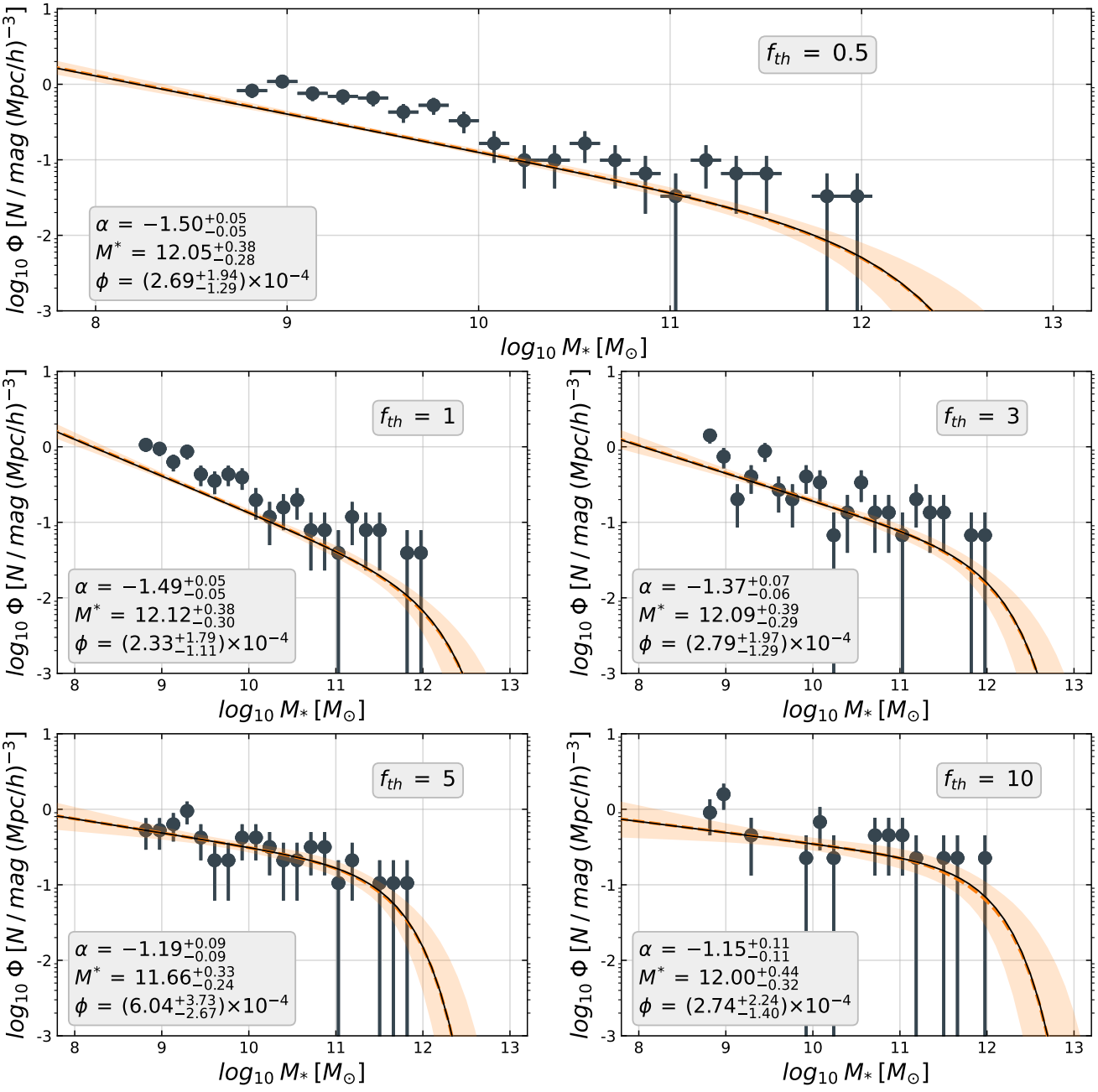

Figure (9) GSMF fits with large-prior at $z = 0.1$ for all the simulations. Fit is done using all data points, but binned for representation. Bars show Poissonian error for each bin. Shaded area is delimited by the uncertainties of α. Best fit values for parameters and their uncertainties are shown in the boxes.

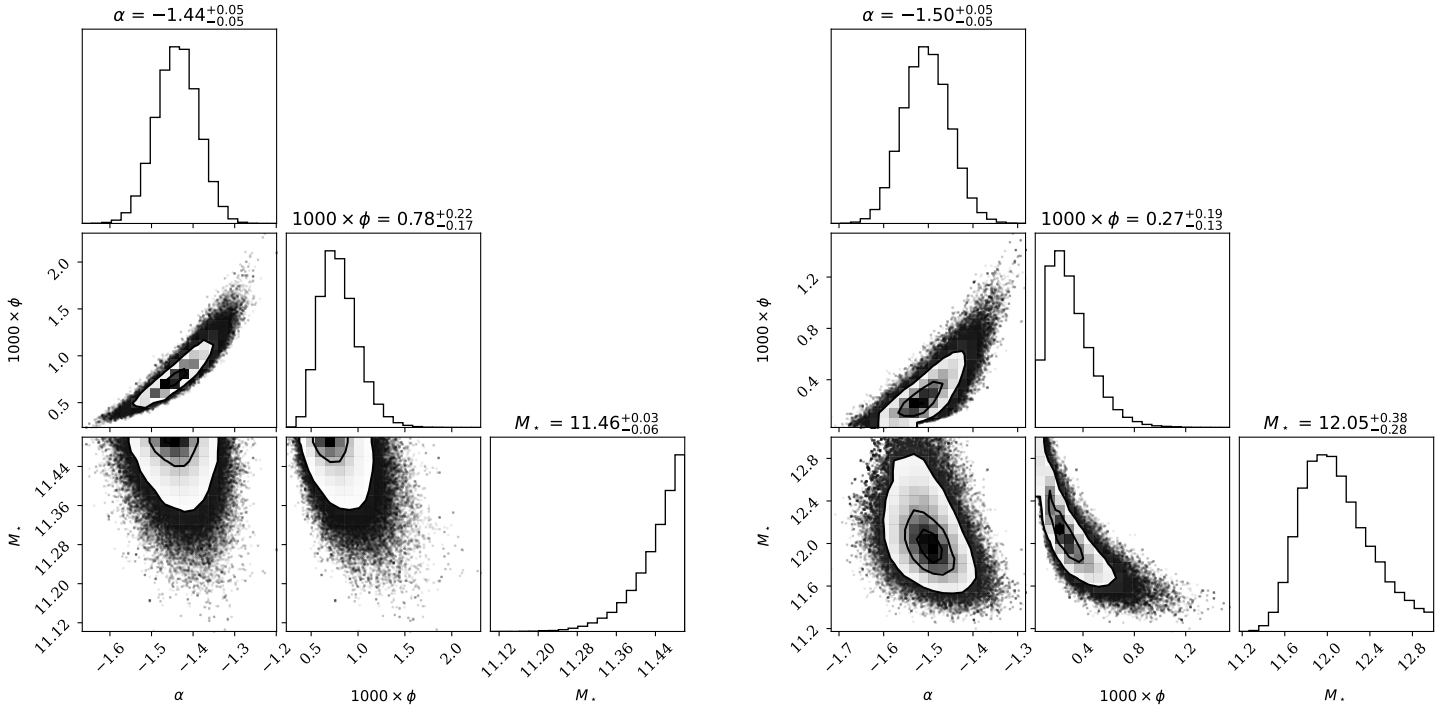

Figure (10) Corners plots for $f_{th} = 0.5$. It shows the relation between fitting parameters in the GSMF, both for the narrow-prior (left) and the large-prior (right). The best fit values and their uncertainties are shown over the boxes

Finally, figure 12 shows the same distribution as 11, but fitted with a double Schechter function. Despite displaying the value of the 5 free parameters, we will focus in the faint ones (represented with the f subscript) because our aim is to analyse the area of the distribution affected by stellar feedback. The values for M^* are much more similar than in the single Schechter case, yet again with the exception of $f_{th} = 5$. With the increased freedom in the fit, α shows a less clear behaviour with efficiency. The slope is almost equal for $f_{th} = 1$ and $f_{th} = 3$, and despite flattening in $f_{th} = 5$, reaches the maximum value for the biggest efficiency. Finally, the fit for $f_{th} = 10$ manifests a weird behaviour, with a local peak at $r = -24$ that indicates a non-physical tendency probably due to excessive degrees of freedom. The posterior distributions and the cross-correlations are shown in the inferior panel in the corner plots in figure 13. Table 2 shows all the best fit parameters, as well as their uncertainties, for each fit and effiency.

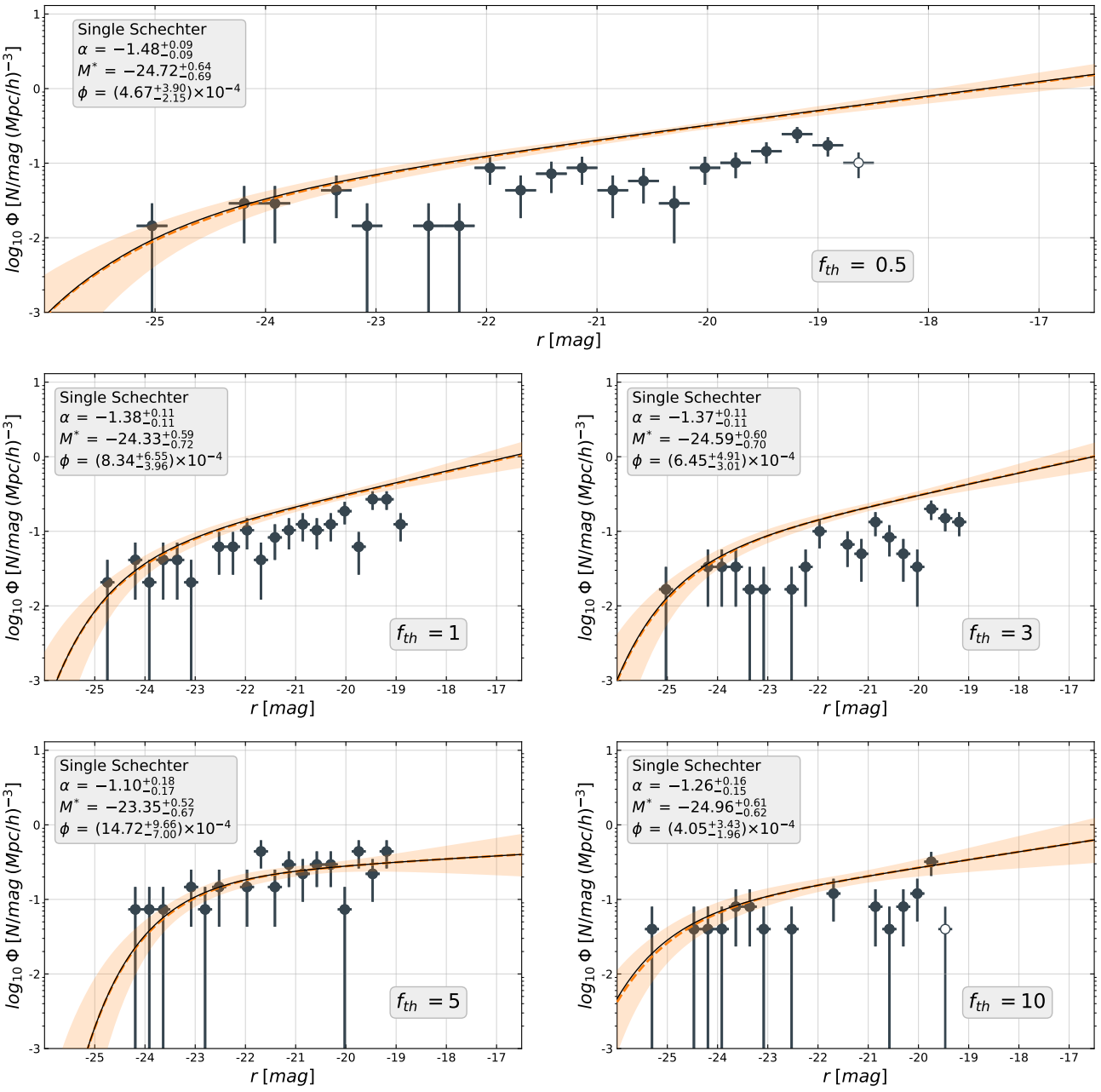

Figure (11) Single Schechter GSLF fits at $z = 0.1$ for all the simulations. Fit is done using all data points, but binned for representation. Bars show Poissonian error for each bin. Shaded area is delimited by the uncertainties of α. Best fit values for parameters and their uncertainties are shown in the boxes.

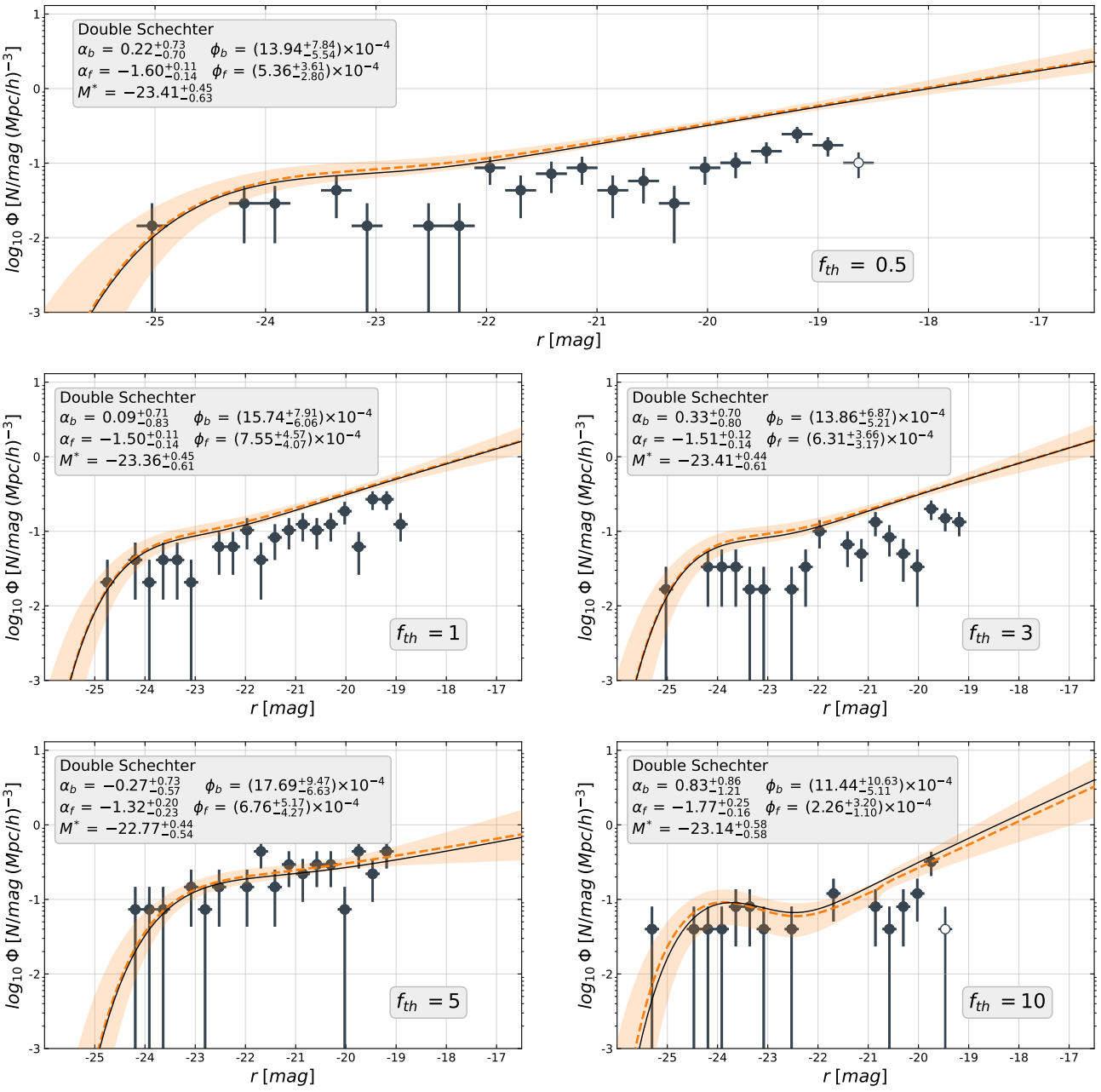

Figure (12) Double Schechter GSLF fits at $z = 0.1$ for all the simulations. Fit is done using all data points, but binned for representation. Bars show Poissonian error for each bin. Shaded area is delimited by the uncertainties of α. Best fit values for parameters and their uncertainties are shown in the boxes.

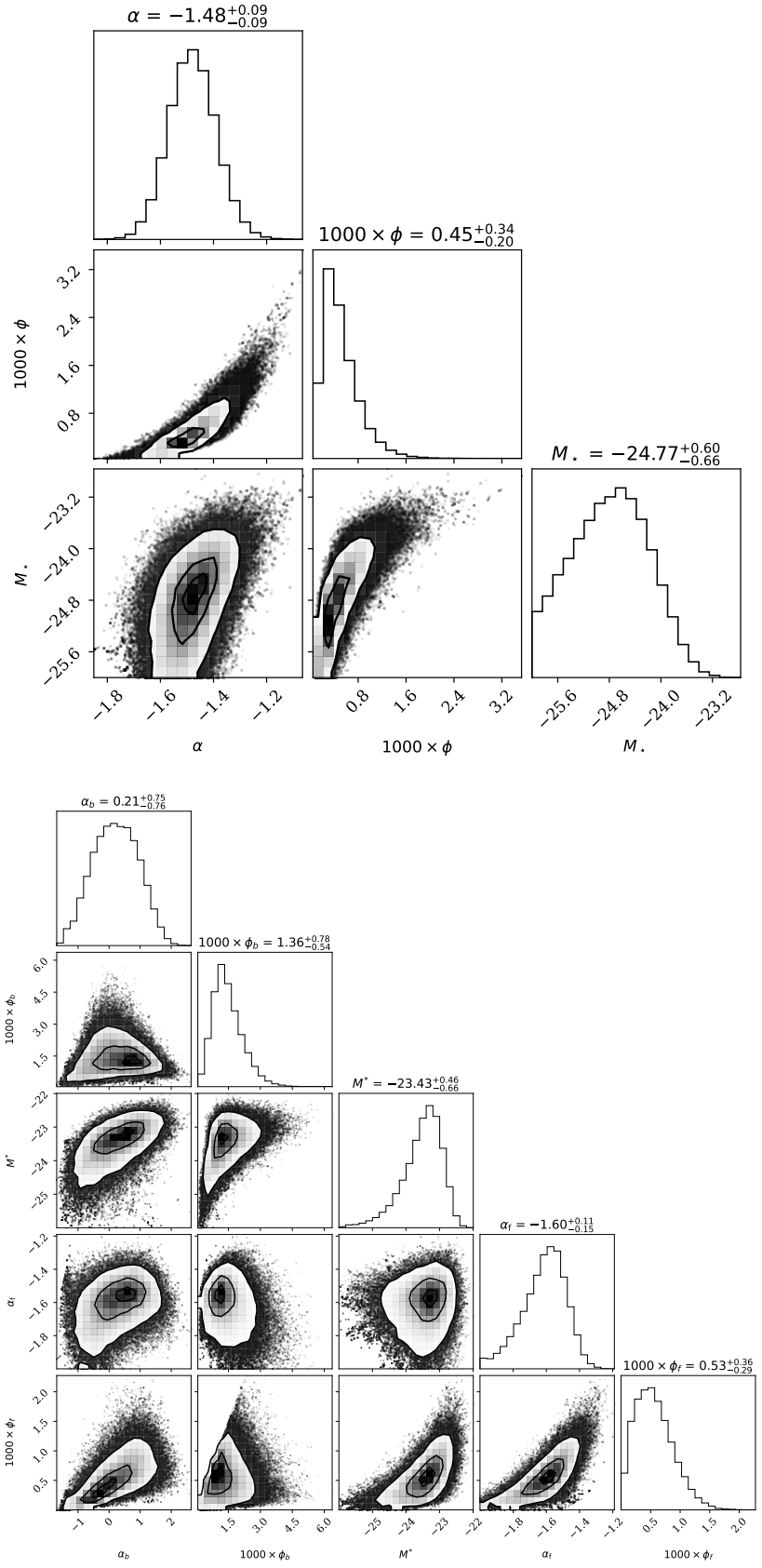

Figure (13) Corners plots for $f_{th} = 0.5$. It shows the relation between fitting parameters in the GSLF, both for the single (up) and the double Schechter (down). The best fit values and their uncertainties are shown over the boxes.

	$f_{th,max}$	0.5	1	3	5	10
α	MF lim.	-1.44 ± 0.05	-1.41 ± 0.05	-1.27 ± 0.06	-1.12 ± 0.08	-1.02 ± 0.11
	MF unlim.	-1.50 ± 0.05	-1.49 ± 0.05	$-1.37^{+0.07}_{-0.06}$	-1.19 ± 0.09	-1.15 ± 0.11
	LF single	-1.48 ± 0.09	-1.38 ± 0.11	-1.37 ± 0.11	$-1.10^{+0.18}_{-0.17}$	-1.26 ± 0.15
	LF double	$-1.60^{+0.11}_{-0.13}$	$-1.50^{+0.11}_{-0.14}$	$-1.51^{+0.11}_{-0.14}$	$-1.32^{+0.20}_{-0.23}$	$-1.77^{+0.25}_{-0.16}$
M^*	MF lim.	$11.46^{+0.03}_{-0.06}$	$11.46^{+0.03}_{-0.06}$	$11.46^{+0.03}_{-0.06}$	$11.39^{+0.07}_{-0.12}$	$11.43^{+0.05}_{-0.09}$
	MF unlim.	$12.05^{+0.38}_{-0.28}$	$12.12^{+0.38}_{-0.30}$	$12.09^{+0.39}_{-0.29}$	$11.66^{+0.33}_{-0.24}$	$12.00^{+0.44}_{-0.32}$
	LF single	$-24.72^{+0.64}_{-0.69}$	$-24.33^{+0.59}_{-0.72}$	$-24.59^{+0.60}_{-0.70}$	$-23.35^{+0.52}_{-0.67}$	$-24.96^{+0.61}_{-0.62}$
	LF double	$-23.41^{+0.45}_{-0.63}$	$-23.36^{+0.45}_{-0.61}$	$-23.41^{+0.45}_{-0.61}$	$-22.77^{+0.44}_{-0.54}$	$-23.14^{+0.58}_{-0.58}$
ϕ ($\times 10^{-4}$)	MF lim.	$7.8^{+2.2}_{-1.7}$	$7.3^{+2.1}_{-1.7}$	$7.7^{+2.5}_{-2.0}$	$9.4^{+3.6}_{-2.7}$	$6.1^{+2.9}_{-2.1}$
	MF unlim.	$2.7^{+1.9}_{-1.3}$	$2.3^{+1.8}_{-1.1}$	$2.8^{+2.0}_{-1.3}$	$6.0^{+3.7}_{-2.7}$	$2.7^{+2.2}_{-1.4}$
	LF single	$4.7^{+3.9}_{-2.1}$	$8.3^{+6.6}_{-4.0}$	$6.5^{+4.9}_{-3.0}$	$14.7^{+9.7}_{-7.0}$	$4.1^{+3.4}_{-2.0}$
	LF double	$5.4^{+3.6}_{-2.8}$	$7.6^{+4.6}_{-4.1}$	$6.3^{+3.7}_{-3.2}$	$6.8^{+5.2}_{-4.3}$	$2.2^{+3.2}_{-1.1}$
α_b	LF double	$0.22^{+0.73}_{-0.70}$	$0.09^{+0.70}_{-0.83}$	$0.33^{+0.70}_{-0.80}$	$-0.27^{+0.73}_{-0.57}$	$0.83^{+0.86}_{-1.21}$
ϕ_b ($\times 10^{-4}$)	LF double	$13.9^{+7.8}_{-5.5}$	$15.7^{+7.9}_{-6.1}$	$13.9^{+6.9}_{-5.2}$	$17.7^{+9.5}_{-6.6}$	$11.4^{+10.6}_{-5.1}$

Table (2) Table containing best fit parameter values for each simulation and function fit at $z = 0.1$. First row show simulation by its efficiency. First column shows fitted parameter. Second row shows function and fit type: MF lim. (Mass Function fit with Schechter limitting $M^* = 10^{11.5}\ M_\odot$), MF unlim. (Mass Function fit with flat prior Schechter), LF single (Luminosity Function fit with single Schechter) and LF double (Luminosity Function fit with double Schechter).

4 Conclusions

When a hydro-cosmological simulation code is developed, the sub-grid physics need to be calibrated to ensure a trustful functioning of the code. In this work, we aim to calibrate the stellar feedback efficiency. For this purpose, we have run and analysed 5 simulations with different stellar feedback efficiencies using the PKDGRAV3 code presented in Asensio et al. (2022). The simulations initially contained 200^3 dark matter and gas particles in a $(13.4\,\mathrm{Mpc/h})^3 = 20^3\ \mathrm{Mpc}^3$ volume and were evolved from $z = 49$ to $z = 0$. The efficiency has been set to the following values: $f_{th,max} = 0.5, 1, 3, 5, 10$. The post-processing included running the FOF and Subfind algorithms to identify galaxies, and computing their magnitudes (section 2.2). The analysis is done using simulation data at $z = 0.1$ for a comparison with observables. The main observables analysed are the star formation history (3.1), the color-stellar mass relation (3.2) and the galactic stellar mass and luminosity functions (3.3). We sum up the general analysis with the following points.

- The full volume SFH shows that (figure 4) the main difference in total star formation happens during the first half of the cosmic time. After $z = 1$, all

the simulations, including the extreme efficiencies ($f_{th} = 0.5$ and 10), converge to a value near $\Psi = 0.1\ M_\odot/\mathrm{yr}\ (\mathrm{Mpc/h})^{-3}$. The only simulation that has a slightly lower star formation in this range is $f_{th} = 5$, probably due to the AGN feedback that is only implemented in this run.

- Before $z = 2$, all the simulations except for $f_{th} = 10$ have a larger SFR than the Madau analytic function (Madau & Dickinson, 2014) used for comparison; $f_{th} = 5$ seems to create the closest total star formation in the first half of the simulated time, but departs most in the second. The rest of the models without AGN feedback seem to agree very well with the comparison function in later times.

- The $g - r$ color-stellar mass relation in figure 5 depicts a lack of red sequence in galaxies with masses over $10^{8.5}\ M_\odot$ for high efficiencies. We set a lower limit for galactic data to be reliable at $10^{8.75}\ M_\odot$, so this indicates that efficiencies $f_{th} = 5$ and 10 are not creating enough quenched galaxies in the $10^9 - 10^{10}\ M_\odot$ range. This feature is related to the low SFR of high efficiencies before $z = 1$.

- We notice that stellar feedback is able to quench star formation in galaxies. The increase in feedback power is directly related to the gap in time between star forming bursts. Low efficiencies, mainly $f_{th} = 0.5$, have a nearly continuous star formation, whereas increasing efficiencies translate into increasingly isolated bursts in the SFH (figure 7).

- The median ages of the red galaxy in figure 7 relate directly with their color in 6. Increasing efficiency traduces into lower medians in the lookback time, which also implies bluer galaxies. Furthermore, we notice the effect of AGN feedback in the color and the median age of simulation $f_{th} = 5$ being lower than in $f_{th} = 3$.

Besides the rather qualitative conclusions just presented, we have some quantitative comparisons with existing literature on the Schechter parameter values derived from the GSMF and GSLF at $z = 0.1$. We use table 1 at Moffett et al. (2016) and table 3 at Loveday et al. (2011) as reference values.

- Concerning the slope of the GSMF, i.e. α, Moffett et al. (2016) yields a value of $\alpha_{ref} = -1.20 \pm 0.016$. For both fits, the narrow- and large-prior ones, the f_{th} that reproduces the observations is between $f_{th} = 3$ and $f_{th} = 5$. For the fit limited at $M^* = 10^{11.5}\ M_\odot$, $f_{th} = 3$ results in $\alpha_{3,NP} = -1.27 \pm 0.06$ and $f_{th} = 5$ in $\alpha_{5,NP} = -1.12 \pm 0.08$. Assuming a linear relation between slope and efficiency in this efficiency range this would result in $f_{th} \approx 4$ being the most

suitable value.

On the other hand, for the large-prior case, $f_{th} = 5$ yields $\alpha_{5,LP} = -1.19 \pm 0.09$, a very close value to the reference. Nevertheless, the fact that $f_{th} = 5$ is the only simulation with AGN feedback activated cannot be ignored. In fact, this favours $f_{th} = 5$, as it is the most complete simulation and reaches a very similar value to Moffett et al. (2016) when no restriction in the fit of the knee is imposed.

- The value for the normalization parameter in Moffett et al. (2016) is $\phi_{ref} = 1.72 \pm 0.12$. This is a value lower than any obtained in both the limited and unlimited case. However, the large-prior fit overall yields smaller values for ϕ, so this could indicate that not limiting the knee is a correct approach in the analysis.

- For the knee magnitude, we have a reference value of $M^*_{ref} = 10^{10.73 \pm 0.033}\, M_\odot$ (Moffett et al., 2016). The narrow-prior fit results in a knee value of $M^*_{NP} \approx 10^{11.5} M_\odot$ for every case, and in the large-prior this increases to $M^*_{LP} \approx 10^{12} M_\odot$. The only exception is $f_{th} = 5$, where the AGN feedback helps to move the knee to lower masses. This brings to light the need to run simulations with AGN feedback on for a more complete analysis.

- Loveday et al. (2011) found $\alpha_{ref,sing} = -1.26 \pm 0.02$ in the r band for the GSLF. This again falls in the interval between $f_{th} = 3$ ($\alpha_{3,sing} = -1.37 \pm 0.11$) and $f_{th} = 5$ ($\alpha_{5,sing} = -1.10^{+0.18}_{-0.17}$), this time closer to the lower efficiency. Focusing in the double Schechter fit, $\alpha_{ref,doub} = -1.47 \pm 0.09$ falls very close to both, $f_{th} = 1$ ($\alpha_{1,doub} = -1.50^{+0.11}_{-0.14}$) and $f_{th} = 3$ ($\alpha_{3,doub} = -1.51^{+0.11}_{-0.14}$). Nevertheless, the effect of AGN feedback over this fit cannot be ignored, as $f_{th} = 5$ yields a bright end slope of $\alpha_{5,b} = -0.27$ while the rest of simulations create a positive slope. However, the uncertainties in this last parameter are huge for all the runs.

- The knee magnitude of our data falls in much larger galaxies than the reference, that yields $M^*_{ref,sing} = -20.73 \pm 0.03$ and $M^*_{ref,doub} = -19.92 \pm 0.010$. None of our values are located under $M^* = -22.5$, highlighting once again the need for AGN feedback. Even so, $f_{th} = 5$ results in $M^*_{5,doub} = -22.77^{+0.44}_{-0.54}$, meaning that even with AGNs, the gap is considerable.

Finally, we present 2 methods regarding future calibrations. We believe that this project, despite resulting in interesting conclusions and giving qualitative and quantitative considerations, can be further improved in the future.

- We have remarked various times in the conclusions, activating AGN feedback in the simulations would help to create a more general picture of the calibration. The lower and higher mass ranges of the GSMF are supposed to be guided by stellar and AGN feedback respectively, but the effect of one on the other cannot be fully disentangled. Relations as the color-stellar mass and the best fit parameter values clearly show that the $f_{th} = 5$ simulation has traits that are directly related to the existence of AGN feedback.

  However, AGN feedback is also controlled by a efficiency parameter (see section 2.1.2), and thus needs to be calibrated. This way, introducing an uncalibrated AGN feedback will result in a degeneracy between both processes, so this will have to be taken into account.

- During the process of calibration, we have considered applying a Bayesian inference method to determine an exact efficiency rather than selecting one of the arbitrary values we chose at the beginning of the process. The main idea is to select an observable that can be represented with a likelihood, e.g. the bayesian fit of the mass function, and compute its posterior for every simulation. Then, extend the hyperspace of the fit parameters by adding the parameter that one wants to calibrate, in our case f_{th}, thus effectively increasing the dimension of the hyperspace. The resulting posterior would be the sum of the posteriors of the different simulations, each one with its own f_{th}. The full posterior (depending on the parameters of the fit and the f_{th}) is then sampled with an MCMC, where the gaps between the different simulations are filled by linearly interpolating between the different runs.

These considerations could not be implemented due to time limitations, but are meant to be useful in the future.

References

Andreon S., Punzi G., Grado A., 2005, Monthly Notices of the Royal Astronomical Society, 360, 727

Asensio I. A., Vecchia C. D., Potter D., Stadel J., 2022, Monthly Notices of the Royal Astronomical Society, 519, 300

Baldry I. K., Glazebrook K., Driver S. P., 2008, , 388, 945

Blanton M. R., Lupton R. H., Schlegel D. J., Strauss M. A., Brinkmann J., Fukugita M., Loveday J., 2005, The Astrophysical Journal, 631, 208

Bondi H., Hoyle F., 1944, , 104, 273

Chabrier G., 2003, , 115, 763

Chiosi C., Bertelli G., Bressan A., 1992, Annual Review of Astronomy and Astrophysics, 30, 235

Cohen M., Wheaton W. A., Megeath S. T., 2003, , 126, 1090

Crain R. A., et al., 2015, , 450, 1937

Crocce M., Pueblas S., Scoccimarro R., 2006, Monthly Notices of the Royal Astronomical Society, 373, 369

Dalla Vecchia C., Schaye J., 2012, , 426, 140

Davis M., Efstathiou G., Frenk C. S., White S. D. M., 1985, , 292, 371

Euclid Collaboration et al., 2021, , 505, 2840

Fukugita M., Ichikawa T., Gunn J. E., Doi M., Shimasaku K., Schneider D. P., 1996, , 111, 1748

Girardi L., Bressan A., Bertelli G., Chiosi C., 2000, VizieR Online Data Catalog, pp J/A+AS/141/371

Gregory P., 2005, Bayesian Logical Data Analysis for the Physical Sciences: A Comparative Approach with Mathematica® Support. Cambridge University Press, Cambridge, UK, doi:10.1017/CBO9780511791277

Hopkins P. F., Raives M. J., 2015, Monthly Notices of the Royal Astronomical Society, 455, 51

Knabenhans M., et al., 2019, Monthly Notices of the Royal Astronomical Society, 484, 5509

Kormendy J., Ho L. C., 2013, Annual Review of Astronomy and Astrophysics, 51, 511

Lanson N., Vila J. P., 2008a, SIAM J. Numerical Analysis, 46, 1935

Lanson N., Vila J.-P., 2008b, SIAM Journal on Numerical Analysis, 46, 1912

Li C., White S. D. M., 2009, , 398, 2177

Loveday J., et al., 2011, Monthly Notices of the Royal Astronomical Society, 420, 1239

Madau P., Dickinson M., 2014, Annual Review of Astronomy and Astrophysics, 52, 415

Moffett A. J., et al., 2016, Monthly Notices of the Royal Astronomical Society, 462, 4336

Negri A., Vecchia C. D., Aguerri J. A. L., Bahé Y., 2022, Monthly Notices of the Royal Astronomical Society, 515, 2121

Potter D., Stadel J., Teyssier R., 2016, PKDGRAV3: Beyond Trillion Particle Cosmological Simulations for the Next Era of Galaxy Surveys (arXiv:1609.08621)

Schaye J., Dalla Vecchia C., 2008, , 383, 1210

Schaye J., et al., 2010, , 402, 1536

Schaye J., et al., 2015, , 446, 521

Schechter P., 1976, , 203, 297

Springel V., Yoshida N., White S. D. M., 2001, , 6, 79

Springel V., et al., 2005, , 435, 629

Springel V., et al., 2008, Monthly Notices of the Royal Astronomical Society, 391, 1685

Springel V., Pakmor R., Zier O., Reinecke M., 2021, Monthly Notices of the Royal Astronomical Society, 506, 2871

Stadel J. G., 2001, PhD thesis, University of Washington, Seattle

Vazdekis A., Koleva M., Ricciardelli E., Röck B., Falcón-Barroso J., 2016, , 463, 3409

and N. Aghanim et al., 2020, Astronomy &amp$$ Astrophysics, 641, A6

van de Schoot R., et al., 2021, Nat Rev Methods Primers, 1, 1